

1 **The effect of temperature-dependent material**
2 **properties on simple thermal models of subduction**
3 **zones**

4 **Iris van Zelst¹, Cedric Thieulot², Timothy J. Craig¹**

5 ¹Institute for Geophysics and Tectonics, School of Earth and Environment, University of Leeds, Leeds,

6 LS2 9JT, United Kingdom

7 ²Department of Earth Sciences, Utrecht University, Utrecht, The Netherlands

8 **Key Points:**

- 9 • We study the effect of temperature-dependent thermal conductivity, heat capac-
10 ity, and density on simple subduction models
- 11 • Using temperature-dependent thermal properties alters the modelled seismogenic
12 zone size and location of dehydration reactions
- 13 • Thermo(-mechanical) models of subduction zones should ideally include temperature-
14 dependent thermal parameters

This manuscript is a preprint which has been submitted for publication.

It has not undergone peer review yet.

Subsequent versions of this manuscript may have slightly different content.

If accepted, the final version of this manuscript will be available

via the 'Peer-reviewed Publication DOI' link on the right - hand side of this webpage. Please feel free to contact any of the authors; we welcome feedback!

Twitter: @iris_van_zelst

15 Abstract

16 To a large extent, the thermal structure of a subduction zone determines where seismicity
 17 occurs through the transition from brittle to ductile deformation and the depth of
 18 dehydration reactions. Thermal models of subduction zones can help understand this
 19 seismicity by accurate modelling of the thermal structure of the subduction zone. Here,
 20 we assess a common simplification in thermal models of subduction zones, i.e., constant
 21 values for the thermal parameters. We use temperature-dependent functions constrained
 22 by lab estimates for the thermal conductivity, heat capacity, and density, to systemat-
 23 ically test their effect on the resulting thermal structure of the slab. To isolate this ef-
 24 fect, we use the well-constrained and thoroughly studied model setup of the subduction
 25 community benchmark by van Keken et al. (2008) in a 2D finite element code. To en-
 26 sure a self-consistent and realistic initial temperature-profile for the slab, we implement
 27 a 1D plate model for cooling of the oceanic lithosphere with an age of 50 Myr in favour
 28 of the previously used half-space model in van Keken et al. (2008). Our results show that
 29 using temperature-dependent thermal parameters in thermal models of subduction zones
 30 result in a cooler plate, which leads to a larger estimated seismogenic zone and a larger
 31 depth at which dehydration reactions responsible for intermediate-depth seismicity oc-
 32 cur. We therefore recommend that thermo(-mechanical) models of subduction take tempera-
 33 ture-dependent thermal parameters into account for accurate modelling of the thermal struc-
 34 ture of subduction zones.

35 Plain Language Summary

36 In a subduction zone, one tectonic plates dives below another one, which is paired with
 37 various forms of seismicity. The maximum size of the earthquakes and the location of
 38 the earthquakes is largely determined by the thermal structure of the subducting plate.
 39 To increase our understanding of seismicity in subduction zones, many studies have mod-
 40 elled this thermal structure. However, one of the common simplifications in the mod-
 41 els is the use of constant thermal parameters in the equations, while lab experiments have
 42 shown that these parameters vary with temperature. Here, we test out various formu-
 43 lations of temperature-dependent thermal parameters to assess the effect on the result-
 44 ing thermal structure of the subduction zone. We find that the thermal structure of a
 45 subducting slab indeed changes when temperature-dependent thermal parameters are
 46 used. More specifically, the subducting plate becomes colder, which results in a differ-
 47 ent potential maximum earthquake magnitude and a changed location for seismicity at
 48 depth. We therefore recommend that modelling studies take the temperature-dependence
 49 of thermal parameters into account to accurately model the thermal structure to pro-
 50 vide some insight into seismicity.

51 1 Introduction

52 The thermal structure of subduction zones plays a vital role in controlling many
 53 geological and petrological processes, including the dehydration of the subducting plate
 54 (Peacock, 2001; Hacker, Abers, & Peacock, 2003), the subsequent hydration of the man-
 55 tle and overriding plate (Peacock, 1993; G. Abers et al., 2017), and mineralogical vari-
 56 ations, including serpentinisation (Hyndman & Peacock, 2003). Furthermore, seismic-
 57 ity can often be related to both the thermal structure, and to various processes controlled
 58 by the pressure and temperature evolution of the slab (Scholz, 2019). For example, interme-
 59 diate-depth earthquakes are associated with a process called dehydration embrittlement (e.g.,
 60 Green & Houston, 1995; Peacock, 2001; Hacker, Peacock, et al., 2003; Yamasaki & Seno,
 61 2003; Jung et al., 2004; Wang et al., 2017). Water is released during the compositional
 62 evolution of the slab, as hydrous minerals progressively transform to less hydrous phases
 63 (e.g., from blueschist to eclogite (van Keken et al., 2011)). The addition of free fluids to
 64 the system acts against the pressure of the surrounding rock, permitting earthquakes to

65 occur at depths where the confining pressure is otherwise too great. These phase tran-
66 sitions are linked to specific temperature and pressure conditions, suggesting that a thor-
67 ough grasp of those conditions at depth could indicate where intermediate-depth seis-
68 micity would be likely to occur (e.g., Hacker, Abers, & Peacock, 2003). Similarly, megath-
69 rust earthquakes occur within the seismogenic zone, the downdip limit of which is thought
70 to be the transition from brittle to ductile deformation (Peacock & Hyndman, 1999; Scholz,
71 2019), and is again controlled, directly or indirectly, by temperature, with isotherms of
72 350–450°C typically linked to this change (Hyndman & Wang, 1993; Hyndman et al.,
73 1997; Gutscher & Peacock, 2003).

74 From these examples, it becomes clear that it is important to have a thorough un-
75 derstanding of the thermal structure of a slab in order to better understand subduction
76 seismicity. However, it is hard to obtain direct observational data on the thermal struc-
77 ture of the slab, due to the inaccessibility of subduction zones and the difficulty of ob-
78 taining data at great depths (i.e., larger than 10 km).

79 The dependence of seismic wavespeeds on temperature allows seismic tomography
80 studies to give a broad overview of the large-scale thermal structure of the subduction
81 zone as a whole, but such studies typically lack the resolution to infer the thermal struc-
82 ture of the slab itself in great detail (e.g., G. A. Abers et al., 2006; Pozgay et al., 2009).
83 In addition, the observed velocity anomalies in tomographic models are not exclusively
84 due to temperature, and wavespeed variations are also related to other factors, partic-
85 ularly composition, density, mineralogy, and the presence of fluids (e.g., Hacker, Abers,
86 & Peacock, 2003; Blom et al., 2017). Whilst bore-hole experiments and marine heat flow
87 measurements can provide vital insights into the thermal state of the shallow seismogenic
88 zone (e.g., Hyndman & Wang, 1993; Chang et al., 2010; Fulton et al., 2013; R. Harris
89 et al., 2013; Yabe et al., 2019), such measurements are extremely local and fail to give
90 a good overview of the conditions of the subduction zone as a whole, especially the finer
91 details of the temperature structure within the slab.

92 In light of the limited available data on the thermal structure of subduction zones,
93 geodynamic numerical modelling provides a way of investigating the complete temper-
94 ature field of subduction zones in relation to the thermal and dynamic evolution of the
95 slab (see Peacock, 2020, for an overview). The starting point for many thermal models
96 of subduction zones are one-dimensional models of the cooling of oceanic lithosphere that
97 define the thermal structure of the slab for a certain plate age, including half-space cool-
98 ing models and more advanced plate models (McKenzie & Sclater, 1969; Parsons & Sclater,
99 1977; Stein & Stein, 1994; Hillier & Watts, 2005; McKenzie et al., 2005; Crosby et al.,
100 2006; Emmerson & McKenzie, 2007; Richards et al., 2018). Extending this thermal mod-
101 elling to two dimensions to study the thermal evolution of a subduction zone in steady
102 state has provided insights into the predicted location of dehydration and melting pro-
103 cesses linked to intermediate-depth seismicity (Ponko & Peacock, 1995; Peacock & Wang,
104 1999; van Keken et al., 2002; G. A. Abers et al., 2006; Syracuse et al., 2010; Van Keken
105 et al., 2012; van Keken et al., 2019). Apart from pure thermal models, thermo-mechanical
106 models with various complexities such as melting and dehydration reactions have also
107 been employed (e.g., T. V. Gerya & Meilick, 2011; T. V. Gerya, 2011; Faccenda et al.,
108 2012; Arcay, 2017; Beall et al., 2021), leading to insights into subduction dynamics and
109 estimates of the depth of intermediate-depth seismicity and the geometry of the megath-
110 rust. When these types of models additionally account for an inertia term in so-called
111 seismo-thermo-mechanical models, megathrust slip events are resolved allowing for es-
112 timates of the maximum size of the seismogenic zone and the distribution of seismicity
113 in a given subduction geometry (van Dinther, Gerya, Dalguer, Mai, et al., 2013; van Dinther,
114 Gerya, Dalguer, Corbi, et al., 2013; van Dinther et al., 2014; Herrendörfer et al., 2015;
115 Van Zelst et al., 2019; Petrini et al., 2020; Brizzi et al., 2020). These types of modelling
116 have the advantage that the temperature can be calculated across the entire subduction
117 zone with arbitrary resolution. However, the results of the model depend on its initial

118 and boundary conditions and the assumptions that enter the model at various stages (van
119 Zelst et al., 2021).

120 Numerical models of the temperature structure of subduction zones are subject to
121 a range of simplifications. One, which we seek to address here, is that the thermal pa-
122 rameters in the model, i.e., the thermal conductivity, heat capacity, and density, are as-
123 summed to be constant or merely material-dependent. In contrast, laboratory experiments
124 have shown that these parameters actually depend on temperature and can differ as much
125 as a factor of 2 depending on the temperature (e.g., Berman, 1988; Berman & Aranovich,
126 1996; Seipold, 1998; A. Hofmeister, 1999; Xu et al., 2004; Wen et al., 2015; Su et al., 2018).
127 The inclusion of such parameters into models for the cooling of oceanic lithosphere has
128 made a significant difference to both the resulting thermal structure, and its interpre-
129 tation and implications (Denlinger, 1992; McKenzie et al., 2005; Richards et al., 2018).
130 Initial one-dimensional studies have highlighted the potential for a similar impact on the
131 more complex thermal structure of subduction zones (Emmerson & McKenzie, 2007).

132 Given the sensitivity of the various processes mentioned above to small-scale vari-
133 ations in the temperature evolution of the slab, we therefore seek to quantify the impact
134 that the incorporation of the temperature-dependence of thermal parameters may have
135 on subduction zone thermal structure, and to build towards their routine incorporation.

136 In order to assess the effect of temperature-dependent thermal parameters on the
137 resulting thermal structure of the slab, we perform a systematic study into this by us-
138 ing the well-constrained setup of the subduction community benchmark by van Keken
139 et al. (2008) with the addition of temperature-dependent functions for the thermal con-
140 ductivity, heat capacity and density as constrained by laboratory experiments (Section 2).
141 We show that using temperature-dependent parameters in geodynamic models signif-
142 icantly changes the resultant thermal structure of the slab, relative to models with fixed
143 values (Section 3). To relate this change in thermal structure to expected seismicity and
144 mineralogical changes in the slab, we discuss the change in the expected depth of intermediate-
145 depth seismicity when temperature-dependent thermal parameters are taken into account
146 (Section 4). Going forwards, we recommend the inclusion of temperature-dependent ther-
147 mal parameters in future thermal models of subduction zones, especially if inferences on
148 seismicity are made.

149 2 Methods

150 We base our models on the subduction zone community benchmark presented by
151 van Keken et al. (2008). We use the tailor-made two-dimensional finite element Python
152 code xFieldstone (*citation of git repository finalised after acceptance of the manuscript*)
153 to solve the incompressible Stokes equations with Crouzeix-Raviart elements and the con-
154 servation of energy using quadratic triangular elements. xFieldstone is based on Field-
155 stone_68 which is part of the open source Fieldstone collection of educational finite el-
156 ement codes in computational geodynamics (<https://cedrict.github.io/>). The ex-
157 act version of xFieldstone used to produce the results presented in this work can be found
158 in the Zenodo repository (*citation of final zenodo repository finalised after acceptance*
159 *of the manuscript*).

160 In the following, we first discuss the governing equations (Section 2.1) and rheol-
161 ogy (Section 2.2) of the physical model. We then present the model setup (Section 2.3),
162 our formulation for the thermal structure of the oceanic plate at the trench on the left-
163 side of the model (Section 2.4), and the different functions we consider for the temperature-
164 dependence of the thermal parameters (Section 2.5). Based on these functions, we de-
165 fine the parameter space of this study (Section 2.6) and detail the model diagnostics used
166 in this work (Section 2.7).

167

2.1 Governing equations

168

169

170

Following van Keken et al. (2008), we solve the incompressible formulation of the conservation of mass and momentum (i.e., the Stokes equations) for velocity \mathbf{v} and pressure p :

$$\nabla \cdot \mathbf{v} = 0, \quad (1)$$

$$\nabla \cdot \boldsymbol{\sigma}' - \nabla p + \rho \mathbf{g} = \mathbf{0}, \quad (2)$$

171

172

173

where $\boldsymbol{\sigma}'$ is the deviatoric stress tensor, ρ is density, and \mathbf{g} is the gravitational acceleration, which we assume to be $\mathbf{0}$ for the purposes of this study. We also solve for temperature T using the steady-state conservation of energy without external heat sources:

$$\rho C_p (\mathbf{v} \cdot \nabla T) - \nabla \cdot (k \nabla T) = 0, \quad (3)$$

174

175

176

where C_p is the heat capacity, and k is the thermal conductivity. Unlike van Keken et al. (2008), we make these thermal parameters temperature-dependent instead of constants, as described in Section 2.5.

177

2.2 Rheology

178

179

180

We consider a purely viscous rheology and hence neglect any elastic and plastic contributions to the deformation. We relate stress to deformation through the deviatoric stress tensor $\boldsymbol{\sigma}'$:

$$\boldsymbol{\sigma}' = 2\eta \dot{\boldsymbol{\epsilon}}, \quad (4)$$

181

where η is the shear viscosity, and $\dot{\boldsymbol{\epsilon}}$ is the strain-rate tensor defined by

$$\dot{\boldsymbol{\epsilon}} = \frac{1}{2} (\nabla \mathbf{v} + \nabla \mathbf{v}^T). \quad (5)$$

182

183

184

185

186

Initially, we run sets of models with different viscous rheologies to successfully reproduce the different benchmark cases presented in van Keken et al. (2008) (Section S1; Figures S1-S7). In the following, we confine ourselves to a rheology that combines the diffusion and dislocation creep mechanisms used in van Keken et al. (2008). We implement this temperature-dependent rheology through an effective shear viscosity η_{eff} .

187

188

189

For the diffusion creep rheology, we use the simplified diffusion creep viscosity formulation η_{diff} for olivine, where we assume zero activation volume and ignore any effect caused by hydration and grain-size dependence:

$$\eta_{\text{diff}} = A_{\text{diff}} \exp\left(\frac{E_{\text{diff}}}{RT}\right), \quad (6)$$

190

191

where A_{diff} is a prefactor, E_{diff} is the activation energy, and R is the universal gas constant. Similarly, we use the following expression for a dislocation creep rheology:

$$\eta_{\text{disl}} = A_{\text{disl}} \exp\left(\frac{E_{\text{disl}}}{nRT}\right) \dot{\boldsymbol{\epsilon}}_{II}^{(1-n)/n}, \quad (7)$$

192 where A_{disl} is a prefactor, n is the power-law exponent and $\dot{\epsilon}_{II} = \sqrt{\dot{\epsilon}_{xx}^2 + \dot{\epsilon}_{xy}^2}$ is the
 193 square root of the second invariant of the deviatoric strain rate tensor (i.e., effective de-
 194 viatoric strain rate).

195 We combine these formulations for diffusion and dislocation creep into one rheol-
 196 ogy by assuming two viscous dampers in series (Schmeling et al., 2008):

$$\eta_{\text{comb}} = \frac{\eta_{\text{diff}} \cdot \eta_{\text{disl}}}{\eta_{\text{diff}} + \eta_{\text{disl}}} = \left(\frac{1}{\eta_{\text{diff}}} + \frac{1}{\eta_{\text{disl}}} \right)^{-1} \quad (8)$$

197 To avoid unrealistically high stresses, we limit the maximum viscosity in the model
 198 to $\eta_{\text{max}} = 10^{26}$ Pa s for both the diffusion and dislocation creep rheology, such that the
 199 effective viscosity η_{eff} becomes

$$\eta_{\text{eff}} = \left(\frac{1}{\eta_{\text{comb}}} + \frac{1}{\eta_{\text{max}}} \right)^{-1}. \quad (9)$$

200 2.3 Model setup

201 We use the two-dimensional model setup of the community benchmark for subduc-
 202 tion zone modelling presented by van Keken et al. (2008) (Figure 1). We consider a do-
 203 main that is $L_x = 660$ km wide and $L_y = 600$ km deep with the origin of the coordi-
 204 nate system at the lower left corner and the y -axis positive upwards. We discretise the
 205 domain by means of a structured triangular grid with a uniform resolution of 2.5 km,
 206 resulting in 528×480 triangular elements. We define a simple slab geometry with a 45°
 207 dip angle originating at the top left corner and a 50 km thick overriding plate at the top
 208 of the model. The remaining part of the model is the mantle wedge. Our chosen reso-
 209 lution ensures that the computational grid aligns with the bottom of the overriding plate
 210 and the wedge corner.

211 We fix the overriding plate by prescribing no slip (i.e., zero velocity in both the x -
 212 and y -direction) at its bottom boundary with the mantle wedge. We define the plate kine-
 213 matics such that the downgoing slab subducts with a constant velocity of 5 cm/year by
 214 prescribing this velocity at the top of the slab from the corner point at $x = 50$ km and
 215 $y = 550$ km to the bottom of the domain. At the corner point itself, we prescribe zero
 216 velocity.

217 For the conservation of energy, we apply a constant 0°C temperature boundary con-
 218 dition along the top of the model domain. At the right-hand boundary, we apply a lin-
 219 ear temperature gradient in the overriding plate from $T = 0^\circ\text{C}$ at the top to 1300°C
 220 at the bottom of the overriding plate at $y = 550$ km. Below that, incoming material
 221 (i.e., $v_x < 0$) is assigned the maximum temperature in the model $T_{\text{max}} = 1300^\circ\text{C}$. At
 222 the left boundary, we apply either a half-space cooling model with a slab age t_s of 50 Myr
 223 and constant thermal parameters (as used in the benchmark of van Keken et al. (2008)),
 224 or a temperature profile extracted at 50 Myr from a one-dimensional cooling plate model
 225 (following Richards et al. (2018), and discussed further in Section 2.4). The initial tem-
 226 perature field is constant with $T = 0^\circ\text{C}$.

227 We first solve the Stokes equations across the entire domain. As we are only inter-
 228 ested in the velocity field in the mantle wedge, we overwrite the resulting velocity so-
 229 lution in the slab and overriding plate by our boundary conditions, i.e., no slip in the
 230 overriding plate and a constant subduction velocity of 5 cm/year in the slip. With the
 231 velocity solution determined, the heat equation is solved next. We then iteratively solve
 232 the Stokes and heat equation until convergence is reached, i.e. when the horizontal and
 233 vertical components of the velocity and the temperature compared to the previous it-
 234 eration change less than a given tolerance. We choose a relative tolerance of 10^{-5} in our

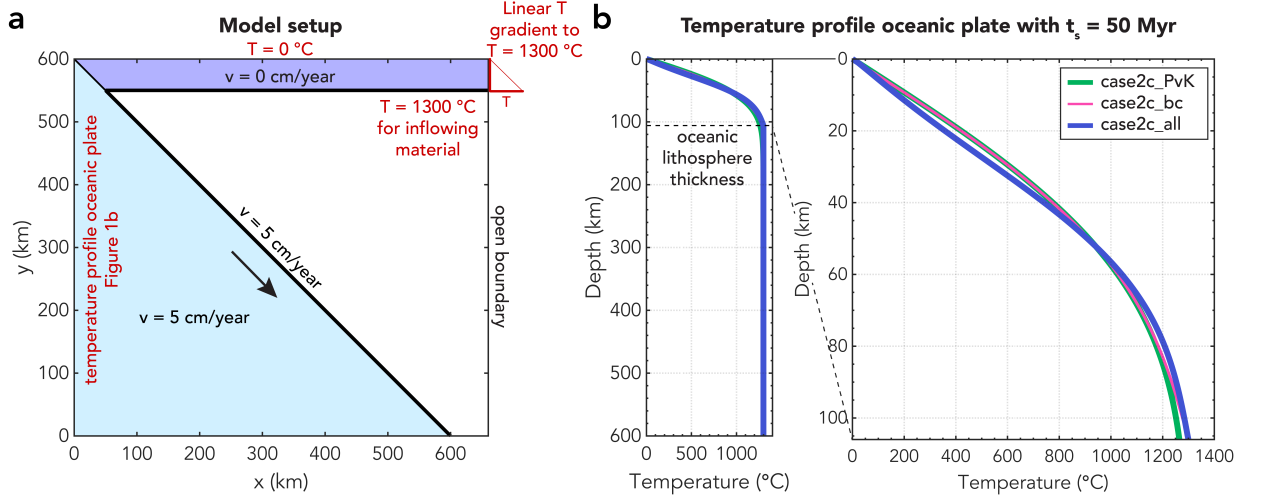


Figure 1. Model setup. (a) Model domain with kinematically prescribed overriding and subducting plate and temperature boundary conditions in red. Black bold lines indicate where we prescribe the velocities at the boundaries of the mantle wedge. (b) Different temperature boundary conditions for an oceanic plate with an age of 50 Myr used at the left-hand side of the model in (a) with a zoom of the top 106 km (i.e., the oceanic lithosphere thickness), below which the temperature is constant at $T = 1300^\circ\text{C}$. The half-space model used by van Keken et al. (2008) is indicated in a thick green line (model case2c.PvK). We also show the two end-member plate models of our parameter study with the plate model with constant thermal parameters in pink (model case2c.bc) and the plate model considering temperature-dependence for all thermal parameters (model case2c.all) indicated in blue. See the supplementary material (Figure S18) for the temperature profiles of all other models.

235 model runs for both velocity and temperature, although we also impose a maximum number of 50 iterations to limit the wall-time of the model. Tests show that employing a lower
 236 tolerance of 10^{-3} (reached before 50 iterations) changes the model diagnostics from Section 2.7 by less than 1°C and has no effect on the reported isotherm depths. To prevent
 237 numerical oscillations in the solution that inhibit convergence of the temperature field,
 238 we limit the change of each new iteration solution via a relaxation parameter r after the
 239 first iteration according to
 240
 241

$$\phi_{\text{new}} = r \cdot \phi_{\text{new}} + (1 - r) \cdot \phi_{\text{old}} \quad (10)$$

242 where ϕ is the solution for v_x , v_y , and T . This relaxation step is applied to the velocity
 243 components after the Stokes solve and to the temperature after the heat equation solve.
 244 After trial and error, we choose $r = 0.8$, which results in robust convergence across our
 245 model runs.

246 2.4 Thermal structure of the oceanic plate at the trench

247 As the left-hand boundary condition for the conservation of energy, we prescribe
 248 the thermal structure of the incoming oceanic plate. In the original community bench-
 249 mark, van Keken et al. (2008) used a simple half-space cooling model (Turcotte & Schu-
 250 bert, 2002) with a plate age of 50 Myr with constant values for the thermal conductiv-
 251 ity, heat capacity, and density:

$$T(y) = T_{\max} \cdot \operatorname{erf} \left(\frac{L_y - y}{2\sqrt{\frac{k}{\rho C_p} t_s}} \right). \quad (11)$$

252 However, the half-space cooling model does not satisfy petrological constraints and
 253 fails to satisfy data for plate ages greater than ~ 80 Ma (Richards et al., 2018). Hence,
 254 we follow Richards et al. (2018) by including a more complex and realistic plate model
 255 as input for the temperature profile of the incoming oceanic plate. This plate model also
 256 has the advantage that it easily incorporates temperature-dependent thermal paramete-
 257 rers, which results in consistency between the thermal structure of the incoming plate
 258 and the thermal structure we solve for in the rest of the domain.

259 We calculate the structure of the incoming oceanic plate in a linked, separate Python
 260 script, with the coordinate convention that the y -axis is positive downwards. The ther-
 261 mal structure of the oceanic plate is based on the one-dimensional heat equation

$$\frac{\partial(\rho C_p T)}{\partial t} = \frac{\partial}{\partial y} \left(k \frac{\partial T}{\partial y} \right). \quad (12)$$

262 Following McKenzie et al. (2005) and Richards et al. (2018), we discretise this equation
 263 using a one-dimensional time- and space-centered Crank-Nicolson finite difference scheme
 264 that is stable in both space and time and solve it numerically with a predictor-corrector
 265 step (Press et al., 1992) according to:

$$\begin{aligned} -A \frac{k_{j-\frac{1}{2}}^m}{\Delta y_{j-1}^m} \cdot T_{j-1}^{n+1} + \left[1 + A \left(\frac{k_{j+\frac{1}{2}}^m}{\Delta y_j^m} + \frac{k_{j-\frac{1}{2}}^m}{\Delta y_{j-1}^m} \right) \right] \cdot T_j^{n+1} - A \frac{k_{j+\frac{1}{2}}^m}{\Delta y_j^m} \cdot T_{j+1}^{n+1} = \\ A \frac{k_{j-\frac{1}{2}}^m}{\Delta y_{j-1}^m} \cdot T_{j-1}^n + \left[1 - A \left(\frac{k_{j+\frac{1}{2}}^m}{\Delta y_j^m} + \frac{k_{j-\frac{1}{2}}^m}{\Delta y_{j-1}^m} \right) \right] \cdot T_j^n + A \frac{k_{j+\frac{1}{2}}^m}{\Delta y_j^m} \cdot T_{j+1}^n + B, \end{aligned} \quad (13)$$

266 with

$$A = \frac{\Delta t}{\rho_j^m C_{p,j}^m (\Delta y_j^m + \Delta y_{j-1}^m)}, \quad (14)$$

267 where $m = n$ for the predictor step and $m = n + \frac{1}{2}$ for the corrector step. Addition-
 268 ally, we have

$$B = -\frac{T_j^n (\rho_j^n C_{p,j}^n - \rho_j^{n-1} C_{p,j}^{n-1})}{\rho_j^n C_{p,j}^n} \quad (15)$$

269 for the predictor step, and

$$B = -\frac{(T_j^{n+1} + T_j^n) (\rho_j^{n+1} C_{p,j}^{n+1} - \rho_j^n C_{p,j}^n)}{\rho_j^{n+1} C_{p,j}^{n+1} + \rho_j^n C_{p,j}^n} \quad (16)$$

270 for the corrector step.

271 As input parameters, we choose a constant Δz of 1000 m and a constant time step
 272 $\Delta t = 1000$ year. We have the same temperature boundary conditions as the 2D model

273 domain for consistency, with a surface temperature of 0°C and a maximum temperature
 274 (mantle potential temperature) of 1300°C. We choose a plate thickness of 106 km in ac-
 275 cordance with the optimum plate thickness found by Parsons and Sclater (1977); Sclater
 276 et al. (1980); McKenzie et al. (2005) based on heat flow observations. We recognise that
 277 this plate thickness diverges from the results of Richards et al. (2018), but their result
 278 involved the inclusions of compositional variability, in addition to the thermal depen-
 279 dence of material properties, which we do not include here. Hence, we use the older plate
 280 thickness value determination of McKenzie et al. (2005).

281 We solve for the temperature evolution of the incoming oceanic plate with the de-
 282 sired thermal parameters (Section 2.5) for 200 Myr, which we store in a lookup table (Fig-
 283 ures S8-S17). The main part of the code then extracts the relevant temperature profile
 284 for a plate age of 50 Myr (van Keken et al., 2008) as input for the left boundary of the
 285 model domain, taking into account the different coordinate system conventions and the
 286 cubic interpolation between the 1D finite difference coordinates and finite element nodes
 287 in case of differing resolutions. We then solve the entire system using tridiagonal elim-
 288 ination.

289 2.5 Temperature-dependent thermal parameters

290 We use temperature-dependent expressions for the thermal conductivity, heat ca-
 291 pacity, and density, using parameterisations based on observational experimental data
 292 for the way in which these values change with changing temperature.

293 Following McKenzie et al. (2005), we approximate the analytical expression for tempera-
 294 ture-dependent thermal conductivity (Figure 2a) by A. Hofmeister (1999) with

$$k_H(T) = \frac{b}{1 + cT} + \sum_{m=0}^3 d_m(T + 273)^m, \quad (17)$$

295 where k has units of $\text{W m}^{-1} \text{K}^{-1}$, although T is in °C in this expression and $b = 5.3$,
 296 $c = 0.0015$, $d_0 = 1.753 \cdot 10^{-2}$, $d_1 = -1.0365 \cdot 10^{-4}$, $d_2 = 2.2451 \cdot 10^{-7}$, and $d_3 = 3.4071 \cdot$
 297 10^{-11} are constants. This expression considers both heat transport and the radiative heat
 298 transfer by phonons.

299 Like McKenzie et al. (2005), we also implement the temperature-dependent con-
 300 ductivity for olivine proposed by Xu et al. (2004) to account for the large uncertainties
 301 in the temperature-dependence of the thermal conductivity:

$$k_X(T) = k_{298} \left(\frac{298}{T + 273} \right)^n. \quad (18)$$

302 where T is in °C, $k_{298} = 4.08 \text{ W m}^{-1} \text{K}^{-1}$ and $n = 0.406$.

303 For the heat capacity (Figure 2b) C_p , we follow Berman (1988) to calculate the heat
 304 capacity of both fayalite and forsterite (McKenzie et al., 2005) such that we have

$$C_{p,\text{fa|fo}} = \left(a_{0,\text{fa|fo}} + a_{1,\text{fa|fo}} \cdot T^{-\frac{1}{2}} + a_{3,\text{fa|fo}} \cdot T^3 \right) \cdot \frac{1000}{m_{\text{fa|fo}}}, \quad (19)$$

305 where C_p is the heat capacity in $\text{J kg}^{-1} \text{K}^{-1}$ and T is in K. We use updated values for
 306 the constants according to Berman and Aranovich (1996), resulting in $a_{0,\text{fa}} = 252$, $a_{1,\text{fa}} =$
 307 $-20.137 \cdot 10^2$, and $a_{3,\text{fa}} = -6.219 \cdot 10^7$ for fayalite and $a_{0,\text{fo}} = 233.18$, $a_{1,\text{fo}} = -18.016 \cdot$
 308 10^2 , and $a_{3,\text{fo}} = -26.794 \cdot 10^7$ for forsterite. To obtain the heat capacity in the cor-
 309 rect unit of $\text{J kg}^{-1} \text{K}^{-1}$, we multiply the equation from Berman (1988) where C_p is in

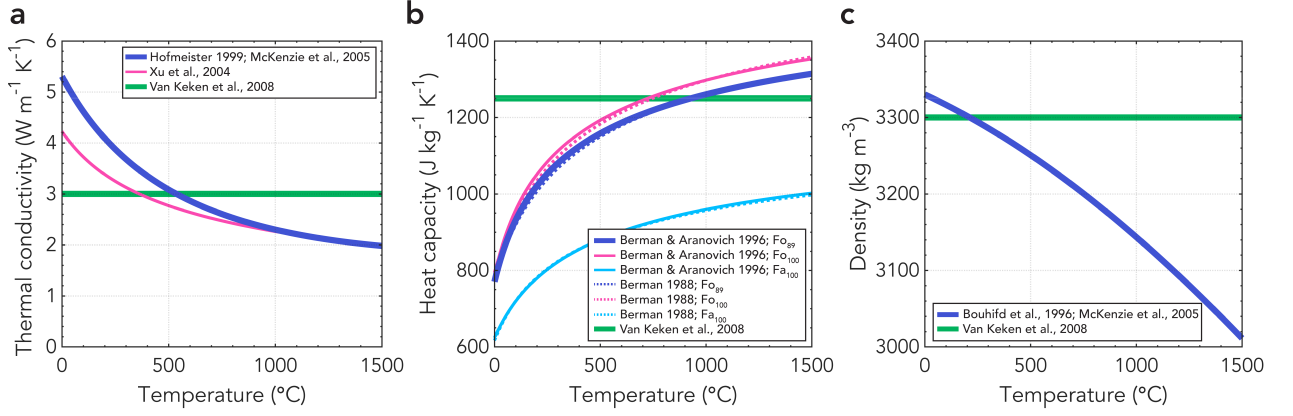


Figure 2. Temperature-dependence of (a) the thermal conductivity k according to Xu et al. (2004) and the approximation of A. Hofmeister (1999) according to McKenzie et al. (2005); (b) the heat capacity C_p according to Berman and Aranovich (1996) (solid lines) and Berman (1988) (dotted lines) for different ratios of forsterite (fo) and fayalite (fa); (c) the density according to the parameterisation by McKenzie et al. (2005) of Bouhifd et al. (1996). Constant values taken from van Keken et al. (2008) are plotted as reference in thick green lines.

310 $\text{J mol}^{-1} \text{K}^{-1}$ with $\frac{1000}{m_{\text{fa|fo}}}$, where $m_{\text{fa|fo}}$ is the molecular mass of fayalite (fa) or forsterite
 311 (fo). We then obtain the effective heat capacity in the model by assuming a molar frac-
 312 tion $f = 0.11$ of fayalite in the mantle according to McKenzie et al. (2005):

$$C_{p,\text{eff}} = (1 - f) \cdot C_{p,\text{fo}} + f \cdot C_{p,\text{fa}}. \quad (20)$$

313 For the dependency of density on temperature (Figure 2c), we follow the param-
 314 eterisation of McKenzie et al. (2005) based on the integration of the parameterisation
 315 of the temperature-dependence of the thermal expansivity according to Bouhifd et al.
 316 (1996):

$$\rho = \rho_0 \exp \left(- \left[\alpha_0 (T - T_0) + \frac{\alpha_1}{2} (T^2 - T_0^2) \right] \right), \quad (21)$$

317 where T is in K, $\rho_0 = 3330 \text{ kg m}^{-3}$, $T_0 = 273.15 \text{ K}$, $\alpha_0 = 2.832 \cdot 10^{-5}$, and $\alpha_1 = 3.79 \cdot$
 318 10^{-8} .

319 Other formulations for the temperature-dependence of the thermal conductivity,
 320 heat capacity, and density than the ones described here are also available (e.g., Berman
 321 & Brown, 1985; Seipold, 1998; Wen et al., 2015; Su et al., 2018), but here we limit our-
 322 selves to the formulations described in this section to test the first-order effect of such
 323 variability.

324 In our preferred formulations for the temperature-dependence of the thermal param-
 325 eters, the thermal conductivity (A. Hofmeister, 1999; McKenzie et al., 2005) varies
 326 with a factor of 2.5 for the temperature range in our subduction zone models (i.e., 0–
 327 1300°C) with $k = 5.3 \text{ W m}^{-1} \text{K}^{-1}$ for $T = 0^\circ\text{C}$ and $k = 2.1 \text{ W m}^{-1} \text{K}^{-1}$ for $T =$
 328 1300°C (Figure 2). Similarly, the heat capacity (89% forsterite Berman & Aranovich,
 329 1996) varies by a factor of 1.65 over the temperature range 0–1300°C. The tempera-
 330 ture-dependence of the density (Bouhifd et al., 1996) is less pronounced, with a variation of
 331 approximately 9% in density for temperatures common to subduction zones.

332

2.6 Parameter space

333

334

335

336

337

338

339

340

341

342

343

344

345

346

347

348

349

350

To systematically test the effect of temperature-dependent parameters on the thermal structure of subduction zones, we run the suite of simulations outlined in Table 1. We start with a reference model case2c_PvK based on the van Keken et al. (2008) benchmark models. Note that this model is not in the original suite of benchmark models of van Keken et al. (2008); the difference being that the rheology employed is a combination of diffusion and dislocation creep. Then, we first test the effect of adding the more complex temperature-profile of the plate model instead of the half-space cooling model in case2c_bc. We test the effect of the two different functions for the thermal conductivity with models case2c_k1 and case2c_k2, where the approximation of the function by A. Hofmeister (1999) is our preferred function, following McKenzie et al. (2005). Our preferred model for the heat capacity is the one where we use the function of Berman (1988) with updated values of Berman (1988) for a composition of 89% of forsterite and 11% fayalite (case2c_Cp6). We also test the effect of using the older values of Berman (1988) (case2c_Cp3), and a composition of 100% forsterite (case2c_Cp4) and 100% fayalite (case2c_Cp5). Here, the numbers behind k and C_p in the model names refer to the flags used in the code to select different options for the temperature-dependent thermal parameters. We test the temperature-dependent density in case2c_rho. Finally, we combine our preferred functions of the thermal parameters in simulation case2c_all.

351

352

353

To illustrate how the different simulations differ in terms of temperature-dependence of the thermal parameters, we show the thermal diffusivity κ in Figure 3 calculated according to

$$\kappa = \frac{k}{\rho C_p}. \quad (22)$$

354

355

356

357

358

359

360

361

362

363

364

Hence, when all thermal parameters k , C_p , and ρ are temperature-dependent in the model case2c_all the overall temperature-dependency of the model is greatest. Compared to the constant thermal diffusivity used in the benchmark by van Keken et al. (2008) values are up to 319% larger and up to 28% smaller for the temperature range of our model. Large values for the diffusivity translate to cold regions heating up faster and hot regions cooling down slower. In general, Figure 3 shows that the thermal diffusivity is higher for low temperatures, meaning that the cold top of the slab will be heated faster. Similarly, the top of the overriding plate is cold, so a large thermal diffusivity will delay the onset of significant heat transfer from the overriding plate to the slab. Note that we do not use the thermal diffusivity within the code as the equations do not allow for this due to the temperature-dependence of the thermal parameters.

365

366

367

368

To illustrate the applicability of our results to the variety of subduction zones observed on Earth, we also run two end-member models with constant and temperature-dependent thermal parameters for a model with a younger ($t_s = 20$ Ma) and older ($t_s = 80$ Ma) slab age, compared to our reference slab age of $t_s = 50$ Ma.

369

2.7 Model diagnostics

370

371

372

373

374

375

376

377

378

To assess our models and quantify their differences, we use the three diagnostics defined in the community benchmark by van Keken et al. (2008), as well as the maximum depth of certain isotherms. Following van Keken et al. (2008), we define a uniform rectangular grid of 111×110 points with 6 km spacing starting in the top left corner and stored row-wise. On this grid, we interpolate the discrete temperature field T_{ij} in $^{\circ}\text{C}$ in a postprocessing step. Using this grid, we output (1) the temperature $T_{x=60\text{km}}$ at the top of the slab at $y = 540$ km and $x = 60$ km, just downdip of the mantle wedge corner; (2) the L2 norm of the temperature along the top of the slab T_{slab} between $y = 600$ km and $y = 390$ km as defined by

Table 1. Simulations^a

Model	T -profile left boundary	k	C_p	ρ	Figures
case2c.PvK	half-space cooling model $t_s = 50$ Myrs	constant	constant	constant	Fig. 4
case2c.bc	plate model $t_s = 50$ Myrs	constant	constant	constant	Fig. S19
case2c.k1	plate model $t_s = 50$ Myrs	McKenzie et al. (2005) approximation of A. Hofmeister (1999)	constant	constant	Fig. S20
case2c.k2	plate model $t_s = 50$ Myrs	Xu et al. (2004)	constant	constant	Fig. S21
case2c.Cp6	plate model $t_s = 50$ Myrs	constant	89% forsterite with values from Berman and Aranovich (1996)	constant	Fig. S22
case2c.Cp3	plate model $t_s = 50$ Myrs	constant	89% forsterite with values from Berman (1988)	constant	Fig. S23
case2c.Cp4	plate model $t_s = 50$ Myrs	constant	100% forsterite with values from Berman and Aranovich (1996)	constant	Fig. S24
case2c.Cp5	plate model $t_s = 50$ Myrs	constant	100% fayalite with values from Berman and Aranovich (1996)	constant	Fig. S25
case2c.rho	plate model $t_s = 50$ Myrs	constant	constant	McKenzie et al. (2005) parameterisation of Bouhfid et al. (1996)	Fig. S26
case2c.all	plate model	McKenzie et al. (2005) approximation of A. Hofmeister (1999)	89% forsterite with values from Berman and Aranovich (1996)	McKenzie et al. (2005) parameterisation of Bouhfid et al. (1996)	Fig. 5
case2c.20PvK	half-space cooling model $t_s = 20$ Myrs	constant	constant	constant	Fig. 8
case2c.20all	plate model $t_s = 20$ Myrs	McKenzie et al. (2005) approximation of A. Hofmeister (1999)	89% forsterite with values from Berman and Aranovich (1996)	McKenzie et al. (2005) parameterisation of Bouhfid et al. (1996)	Fig. 8
case2c.80PvK	half-space cooling model $t_s = 80$ Myrs	constant	constant	constant	Fig. 8
case2c.80all	plate model $t_s = 80$ Myrs	McKenzie et al. (2005) approximation of A. Hofmeister (1999)	89% forsterite with values from Berman and Aranovich (1996)	McKenzie et al. (2005) parameterisation of Bouhfid et al. (1996)	Fig. 8

^a The constant values used for the thermal conductivity k , heat capacity C_p , and density ρ are taken from van Keken et al. (2008) to be $k = 3 \text{ W m}^{-1} \text{ K}^{-1}$, $C_p = 1250 \text{ J kg}^{-1} \text{ K}^{-1}$, and $\rho = 3300 \text{ kg m}^{-3}$.

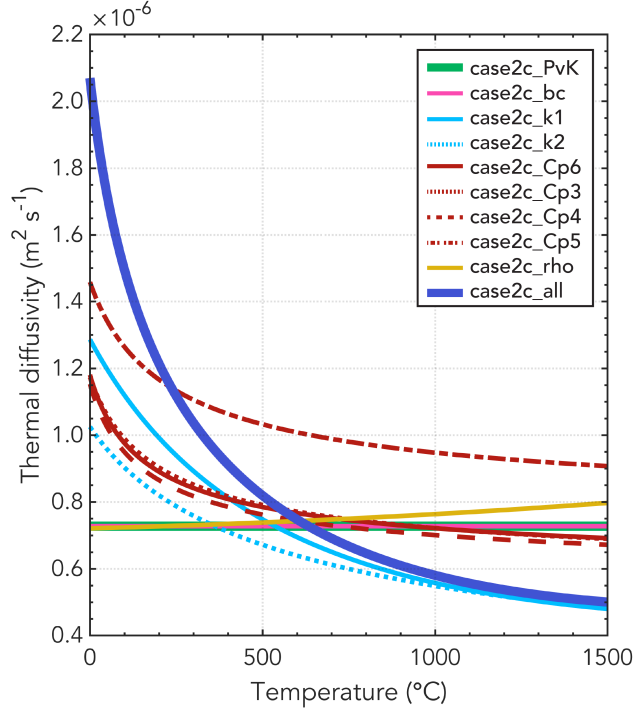


Figure 3. The thermal diffusivity κ for all the simulations (Table 1), which indicates the overall temperature-dependence of the model by combining the thermal conductivity k , heat capacity C_p , and density ρ according to $\kappa = \frac{k}{C_p \rho}$.

$$T_{\text{slab}} = \sqrt{\frac{\sum_{i=1}^{36} T_{ii}^2}{36}}; \quad (23)$$

379 and (3) the L_2 norm of the temperature in the tip of the mantle wedge between 54 and
380 120 km depth as defined by

$$T_{\text{wedge}} = \sqrt{\frac{\sum_{i=10}^{21} \sum_{j=10}^i T_{ij}^2}{78}}. \quad (24)$$

381 In addition to the diagnostics previously used in (van Keken et al., 2008), we fur-
382 ther report additional diagnostics that relate more closely to changes in the thermal struc-
383 ture that impact on other process, particularly the main processes governing seismoge-
384 nesis. We report the maximum depth of the 350°C and 450°C isotherms within the slab,
385 which are associated with the brittle-ductile transition and hence the downdip limit of
386 the seismogenic zone of megathrust seismicity (Hyndman et al., 1997; Gutscher & Pea-
387 cock, 2003). We also report the maximum depth of the 600°C isotherm in the slab, which,
388 together with the 350°C and 450°C isotherms, is associated with the main dehydration
389 reaction fronts within the slab, and the associated intermediate-depth seismicity between
390 70 km and 350 km depth (Peacock, 2001; Yamasaki & Seno, 2003; Kelemen & Hirth, 2007).

391 We also provide snapshots of relevant variables, such as the temperature, viscos-
392 ity, and velocity. Postprocessing and visualisation is primarily done using Matlab scripts

393 (available in the Zenodo directory) with additional touch-ups in Adobe Illustrator. We
 394 use scientific colour maps by Cramer (2018b); Cramer et al. (2020) to avoid visual dis-
 395 tortion of the data and exclusion of readers with colour-vision deficiencies (Cramer, 2018a).
 396 To compare the thermal parameters and initial temperature conditions of the different
 397 models, we colour the models according to the optimal qualitative colour palette by Anton
 398 Tsitsulin (2019; retrieved: May 10, 2021).

399 **3 Results**

400 **3.1 Models with constant thermal parameters**

401 The results from the reference model case2c.PvK with constant thermal param-
 402 eters are shown in Figure 4. It shows a subducting plate with a relatively cold core and
 403 a cold overriding plate with the base of the overriding plate that spills into the mantle
 404 wedge. There is flow in the mantle wedge around the base of the overriding plate which
 405 reaches the tip of the mantle wedge at $x = 50$ km and $y = 550$ km and heats up the
 406 subducting plate from the top.

407 The reference model has a combined dislocation and diffusion creep rheology in con-
 408 trast to the original cases presented in van Keken et al. (2008) which are either isovis-
 409 cous (Figures S1-S4), purely diffusion creep (Figure S6), or purely dislocation creep (Fig-
 410 ure S7). Despite the difference in rheology, the model diagnostics of our reference model
 411 do not change significantly with respect to the model with a pure dislocation or diffu-
 412 sion creep rheology presented in van Keken et al. (2008) (Figure S5). However, looking
 413 at the snapshots presented in Figure 4 and comparing them to the benchmark models
 414 of van Keken et al. (2008) (Figure S6,7), there are distinct differences between our ref-
 415 erence model and the benchmark cases presented in van Keken et al. (2008) in terms of
 416 the viscosity and velocity field in the mantle wedge, as well as the temperature field within
 417 the slab. These differences are not evident from our quantitative model diagnostics, as
 418 the differences manifest themselves at high temperatures in the mantle wedge. These high
 419 temperatures and the region of the mantle wedge are not included in our model diag-
 420 nostics, as they principally affect the area of the model domain outside the main focus
 421 of our study, i.e., the slab.

422 In model case2c.bc, we build upon our reference model and change the initial and
 423 boundary temperature condition of the subducting oceanic plate at the left of the model
 424 from a half-space cooling model to the plate model. This does not incur major changes
 425 in the model diagnostics (Table 2), consistent with the similarity between the temper-
 426 ature profiles of the half-space cooling model and the plate model with constant values
 427 for the thermal parameters (Figure 1b).

428 **3.2 Models with temperature-dependent thermal conductivity**

429 Using the temperature-dependent thermal conductivity according to A. Hofmeis-
 430 ter (1999); McKenzie et al. (2005) in model case2c.k1 results in an overall colder model
 431 with the slab isotherms penetrating deeper into the mantle. This effect increases with
 432 temperature with the 350°C isotherm reaching 20 km deeper into the mantle and the
 433 600°C isotherm reaching almost 90 km deeper into the mantle compared to the refer-
 434 ence model (Figure 7). We observe a similar but less-pronounced trend when we use the
 435 thermal conductivity by Xu et al. (2004).

436 **3.3 Models with temperature-dependent heat capacity**

437 When using a temperature-dependent heat capacity, the model diagnostics show
 438 larger temperatures in the mantle wedge compared to the reference model with a con-
 439 stant heat capacity value. Similarly, the subducting slab is warmer and isotherms pen-

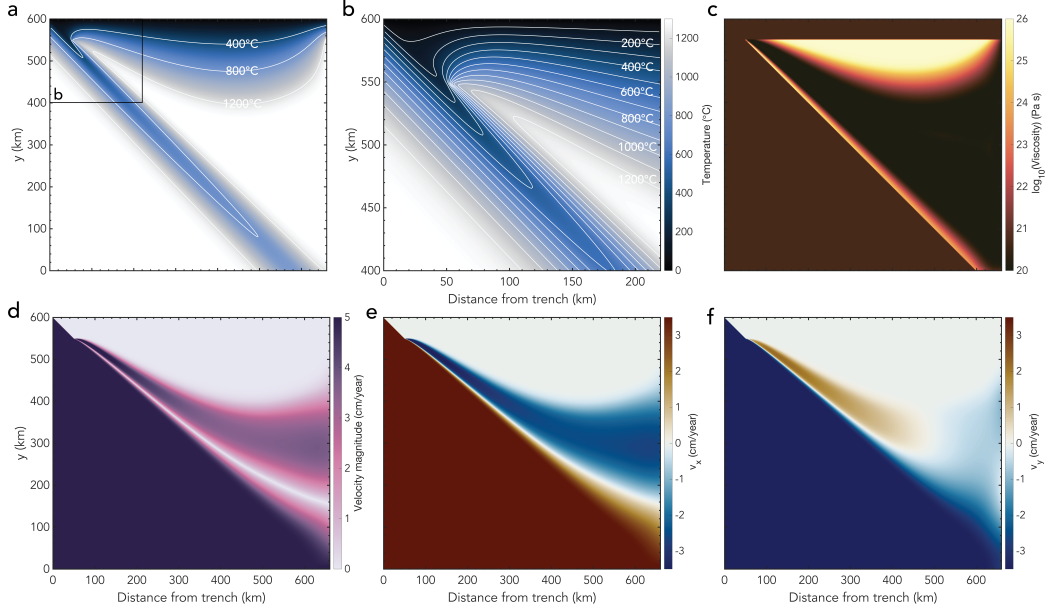


Figure 4. Snapshots of different variables for model case2c_PvK with constant values for the thermal parameters based on van Keken et al. (2008) but including both a dislocation and diffusion creep rheology (Table 1). (a) Temperature field with isotherms indicated in white; (b) zoom of the temperature field; (c) viscosity; (d) velocity magnitude; (e) horizontal component of the velocity; (f) vertical component of the velocity.

440 etrate less deep into the mantle. For our preferred heat capacity model with 89% forsterite
 441 and values from Berman and Aranovich (1996), the temperature diagnostics in the man-
 442 tle wedge are larger by up to 37.7°C and the maximum depths reached by the isotherms
 443 in the slab are shallower by 13.7 - 50 km (Figure 7).

444 Using the values of Berman (1988) instead of the updated values of Berman and
 445 Aranovich (1996) only incurs minor changes in the model diagnostics of maximum 0.9°C
 446 and 1.3 km. Changing the ratio of forsterite and fayalite to 100% forsterite in model case2c_Cp4
 447 results in a slightly warmer mantle wedge by up to 2.8°C and shallower slab isotherms
 448 identical to the isotherm depths obtained in model case2c_Cp3 with values from Berman
 449 (1988) (Figure 7). In the purely fayalite model case2c_Cp5, the heat capacity is signif-
 450 icantly lower, resulting in the model that is cooler than the model with 89% forsterite
 451 (case2c_Cp6), but still warmer than the reference model with a constant value for the
 452 heat capacity. Disregarding the temperature-dependent aspect of heat capacity tested,
 453 the overall magnitudes of the heat capacity used in the four C_p models from Figure 2b
 454 also differs. For example, the pure fayalite heat capacity model has the lowest overall
 455 heat capacity. This trend in changing magnitude of the heat capacity is also consistently
 456 visible in the model results with models with lower heat capacity exhibiting lower tem-
 457 peratures and models with higher heat capacity resulting in higher temperature diag-
 458 nostics. However, it is not straightforward to include the model with constant heat ca-
 459 pacity values in this trend as well. For example, model case2c_Cp5 with fayalite values
 460 consistently has a lower heat capacity than the reference model with constant values, but
 461 the overall model diagnostics still show larger temperatures like the models with both
 462 larger and smaller heat capacity magnitudes depending on the temperature. Hence, the
 463 temperature-dependence of the heat capacity has non-linear effects on the resulting tem-
 464 perature field.

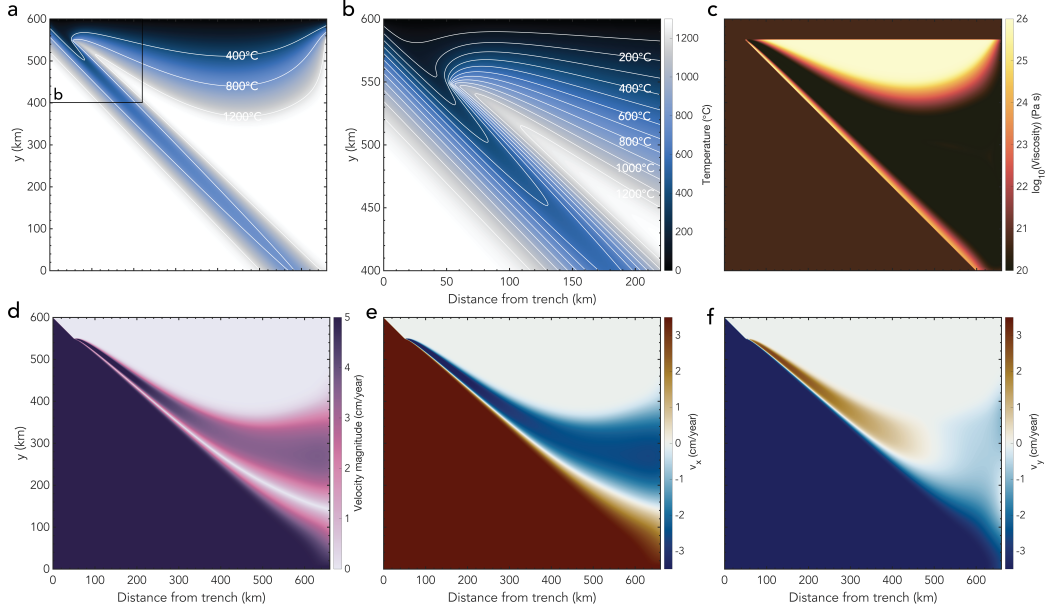


Figure 5. Snapshots of different variables for model case2c-all with our preferred temperature-dependent functions for all thermal parameters k , C_p , and ρ (Table 1). (a) Temperature field with isotherms indicated in white; (b) zoom of the temperature field; (c) viscosity; (d) velocity magnitude; (e) horizontal component of the velocity; (f) vertical component of the velocity.

465

3.4 Models with temperature-dependent density

466

467

468

469

When we use a temperature-dependent density in model case2c_rho the model is cooler than the reference model case2c_PvK, but the effect is less pronounced than for the thermal conductivity (Table 2; Figure 7). This results in isotherms that reach deeper into the mantle.

470

471

3.5 Models including all three temperature-dependent thermal parameters

472

473

474

475

476

477

478

479

480

481

482

483

484

485

486

487

488

We show the results for the model case2c_all in Figure 5. In this model, we include the temperature-dependent function for the thermal conductivity by A. Hofmeister (1999); McKenzie et al. (2005), the function of the heat capacity for 89% forsterite with values from Berman and Aranovich (1996), and the temperature-dependent density. We show the differences between this model and the reference model (Figure 4) in Figure 6 for easy comparison. Based on our model diagnostics (Table 2), the model is overall colder than the reference model and the slab has a colder core with isotherms that reach deeper into the mantle when we use temperature-dependent expressions for all thermal parameters (Figure 7). However, the effect is less pronounced than for the models where we only use a temperature-dependent expression for the thermal conductivity. This is likely because the warming effect of the temperature-dependent heat capacity cancels part of the cooling effect of using temperature-dependent thermal conductivity and density. The largest difference between the two models is due to the overriding plate, which is colder in the temperature-dependent model. Although we specifically focus on the change in thermal structure in the slab in this work, the extreme effect in the overriding plate indirectly affects the thermal structure of the slab. Since the overriding plate is colder in models including temperature-dependence of the thermal parameters, the heating of the inter-

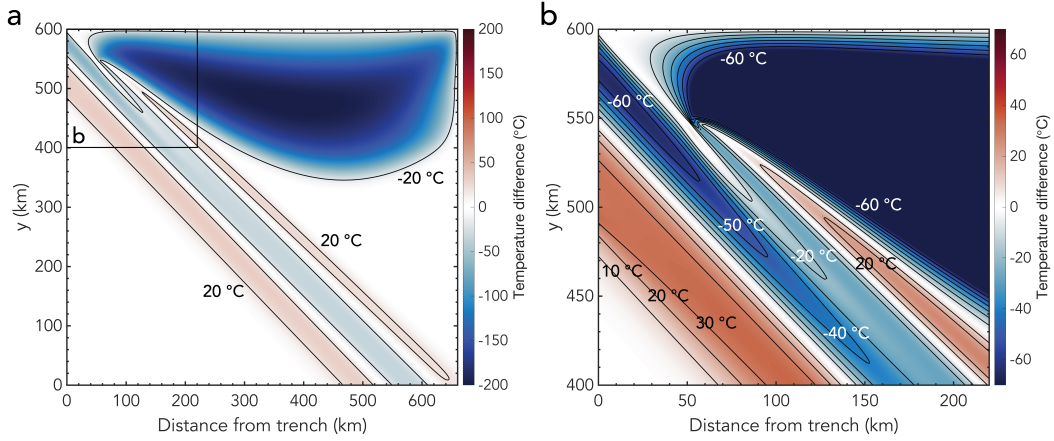


Figure 6. (a) Difference in temperature field between model case2c_all (Figure 5) and model case2c_PvK (Figure 4) with (b) a zoom of the top left corner of the model. Contours of the temperature difference are indicated in black. Note that panel (b) has a different colour scale than panel (a) to highlight the differences between the two models within the slab.

489 face between the slab and the overriding plate will be delayed, which will likely play an
 490 important role in time-dependent models of the thermal evolution of slab dynamics. Within
 491 the slab itself, Figure 6 shows that the largest temperature differences are approximately
 492 -65°C in the shallow part. The top of the slab is colder in model case2c_all, allowing
 493 isotherms to reach deeper into the mantle. The difference in isotherm depth is 3.8 km
 494 for the 350°C isotherm, 10 km for the 450°C isotherm, and 28.8 km for the 600°C isotherm
 495 (Figure 7). At the base of the lithosphere the bottom of the slab is warmer by up to 35°C
 496 compared to the reference model.

497 To summarise the effect of using temperature-dependent thermal parameters for
 498 all our models with a plate age of 50 Myr, we plot the maximum depth of the 350°C ,
 499 450°C , and 600°C isotherms for each model in Figure 7. With respect to the reference
 500 model with constant values, adding the temperature-dependent thermal conductivity by
 501 A. Hofmeister (1999); McKenzie et al. (2005) results in the largest changes in isotherm
 502 depth, with the isotherms reaching greater depths. Using a temperature-dependent den-
 503 sity also results in a colder top of the slab with deeper isotherms. In contrast, using a
 504 temperature-dependent heat capacity yields a warmer slab with isotherms penetrating
 505 the mantle less deep than the reference model. Combining the effect of temperature-dependent
 506 thermal conductivity, heat capacity, and density results in an overall effect of slab cool-
 507 ing with the isotherms reaching greater depths.

508 3.6 Models with different slab ages

509 Similar to the models with a plate age of 50 Myr, we see a cooling effect in the temperature-
 510 dependent thermal models for the models with different plate ages (Figure 8), with the
 511 changes to the thermal structure of the slab more pronounced with increasing slab age.
 512 Similarly, from Figure 9, we see that there is a particularly strong trend when it comes
 513 to larger isotherms such as 600°C with the differences between the reference models in-
 514 cluding constant thermal parameters and the models with variable properties increas-
 515 ing when the plate gets older. Hence, including temperature-dependent thermal param-
 516 eters has a larger effect for old, cold subducting plates. This is expected, as the func-
 517 tions used in this paper for temperature-dependent thermal properties (Figure 2) have

Table 2. Model diagnostics for all simulations

	$T_{x=60\text{km}}$ (°C)	T_{slab} (°C)	T_{wedge} (°C)	Max depth 350°C (km)	Max depth 450°C (km)	Max depth 600°C (km)
case2c_PvK	578.5	604.9	999.5	77.5	110.0	203.8
case2c_bc	578.4	604.8	999.5	77.5	110.0	203.8
case2c_k1	526.0	553.6	948.9	97.5	148.8	291.3
case2c_k2	549.8	573.0	975.3	90.0	135.0	260.0
case2c_Cp6	616.2	642.4	1007.6	63.8	87.5	153.8
case2c_Cp3	616.9	643.3	1007.8	63.8	86.3	152.5
case2c_Cp4	618.9	644.0	1010.4	63.8	86.3	152.5
case2c_Cp5	588.4	626.1	979.0	66.3	91.3	161.3
case2c_rho	566.6	593.7	992.0	81.3	117.5	221.3
case2c_all	552.6	581.6	949.8	81.3	120.0	232.5
case2c_20PvK	631.8	670.6	1008.6	53.8	70.0	108.8
case2c_20all	602.9	643.9	957.9	78.8	97.5	125.0
case2c_80PvK	558.5	578.9	996.0	97.5	148.8	293.8
case2c_80all	533.6	556.9	946.6	102.5	162.5	333.8

518 their most extreme values at lower temperatures, which are more prevalent in older, and
519 hence colder, slabs.

520 4 Discussion

521 Our results clearly show that temperature-dependent thermal parameters signif-
522 icantly affect the thermal structure of the slab in these simple models of subduction zones.
523 Our models with different plate ages show that the implications generalise to all subduc-
524 tion zones regardless of plate age, but they still lack realism in terms of model geome-
525 try and the inclusion of many important processes relevant for the development of a re-
526 listic thermal structure of the slab.

527 In this section, we first discuss the implications of our results on modelling the ther-
528 mal structure of subduction zones in light of megathrust, intermediate-depth, and deep
529 seismicity while taking into account the simple nature of our models (Section 4.1). As
530 our models are conceptual calculations for the impact of including temperature-dependent
531 variables, these implications are generic, rather than applicable directly to any given sub-
532 duction zone (van Zelst et al., 2021). We further discuss the potential implications of our
533 thermal models for the geochemical and mineralogical evolution of the slab, and the im-
534 pact this may have on the flux of fluids through subduction zones (Section 4.2). We then
535 discuss how realistic our models are, their limitations, and how future work could im-
536 prove both the models, and their applicability (Section 4.3).

537 4.1 Implications for seismicity

538 The temperature structure of a slab determines to a large extent where seismic-
539 ity is expected to occur, through its effect on both the mode of failure and the onset of
540 ductility, and its control on geochemical transitions within the slab and along the megath-
541 rust interface, including dehydration reactions. Here we summarise those effects and high-
542 light how the results presented in Section 3 translate to influences on the distribution
543 and extent of intermediate-depth and deep-focus earthquakes, and potentially on the ex-
544 tent of megathrust and related shallow seismicity.

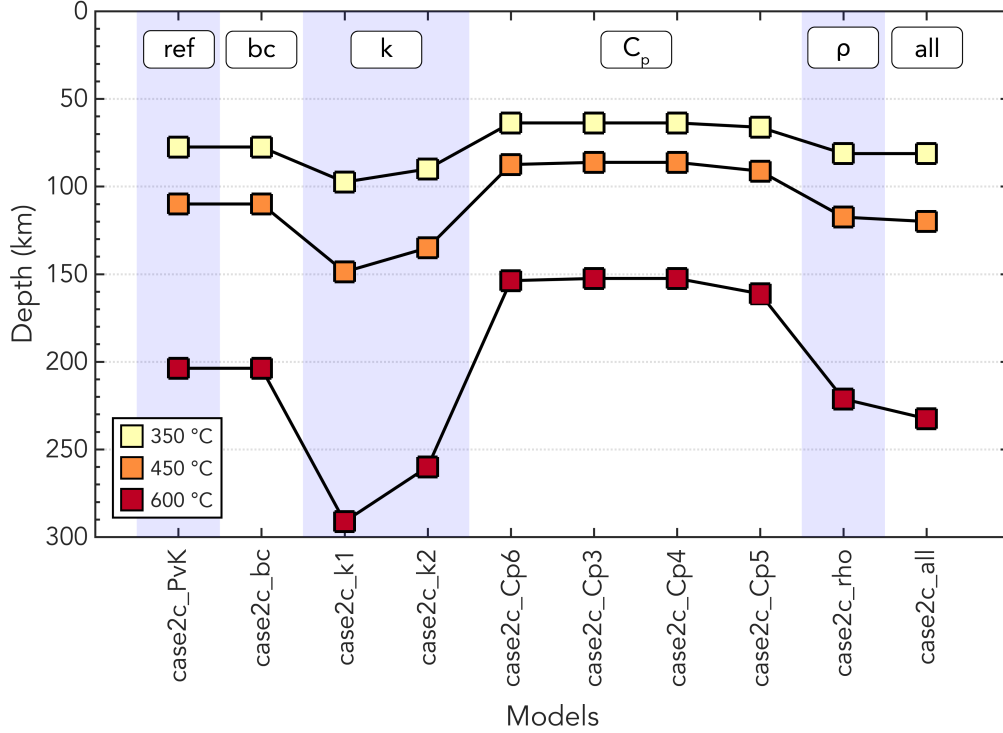


Figure 7. Change in maximum isotherm depth within the slab for models with different variations of temperature-dependent thermal parameters (Table 1). The three isotherm depths plotted here are the same as the ones from the model diagnostics in Table 2. Different groups of models (i.e., testing different functions for the temperature-dependence of the thermal conductivity k) are indicated by vertical bands for clarity. Here, ‘ref’ refers to the reference model case2c_PvK.

545

4.1.1 Intermediate-depth seismicity

546

547

548

549

550

551

552

553

554

555

556

557

558

559

560

561

562

563

564

565

Although the shallow slab geometry in our model is clearly a simplification, at depths consistent with intermediate-depth seismicity, the slab dip of 45° in our models is realistic, with an average slab dip of 45.5° reported by Syracuse et al. (2010) in nature, although it remains highly variable between different subduction zones. Other studies also find that the slab dip is steeper away from the interface between the slab and the over-riding plate (e.g., Jarrard, 1986; King, 2001; Hu & Gurnis, 2020). Therefore, we can make some inferences on the expected depth of intermediate-depth seismicity using our models. Intermediate-depth seismicity at depths of 75 - 300 km is commonly associated with a temperature range between 600°C and 800°C , where dehydration embrittlement of the metamorphosed minerals in the slab occurs (e.g., Jung et al., 2004; Wang et al., 2017). Focusing on the 600°C isotherm in our models (Table 2; Figure 7), we see that its depth changes significantly throughout our parameter space with a depth of 203.8 km for the reference model case2c_PvK, 232.5 km for model case2c_all, and end members of 291.3 km depth for model case2c_k1 and 152.5 km depth for models case2c_Cp3 and case2c_Cp4. Hence, the depth at which dehydration reactions are expected to occur varies by almost 140 km within our parameter space. Therefore, the predicted depth of intermediate-depth seismicity in thermal models of subduction should be viewed in light of the assumptions on the thermal parameters. In addition, previous thermal models (e.g., Syracuse et al., 2010; Van Keken et al., 2012) that use constant values for the thermal parameters and reproduce a thermal structure that fits observed seismicity are expected to change when

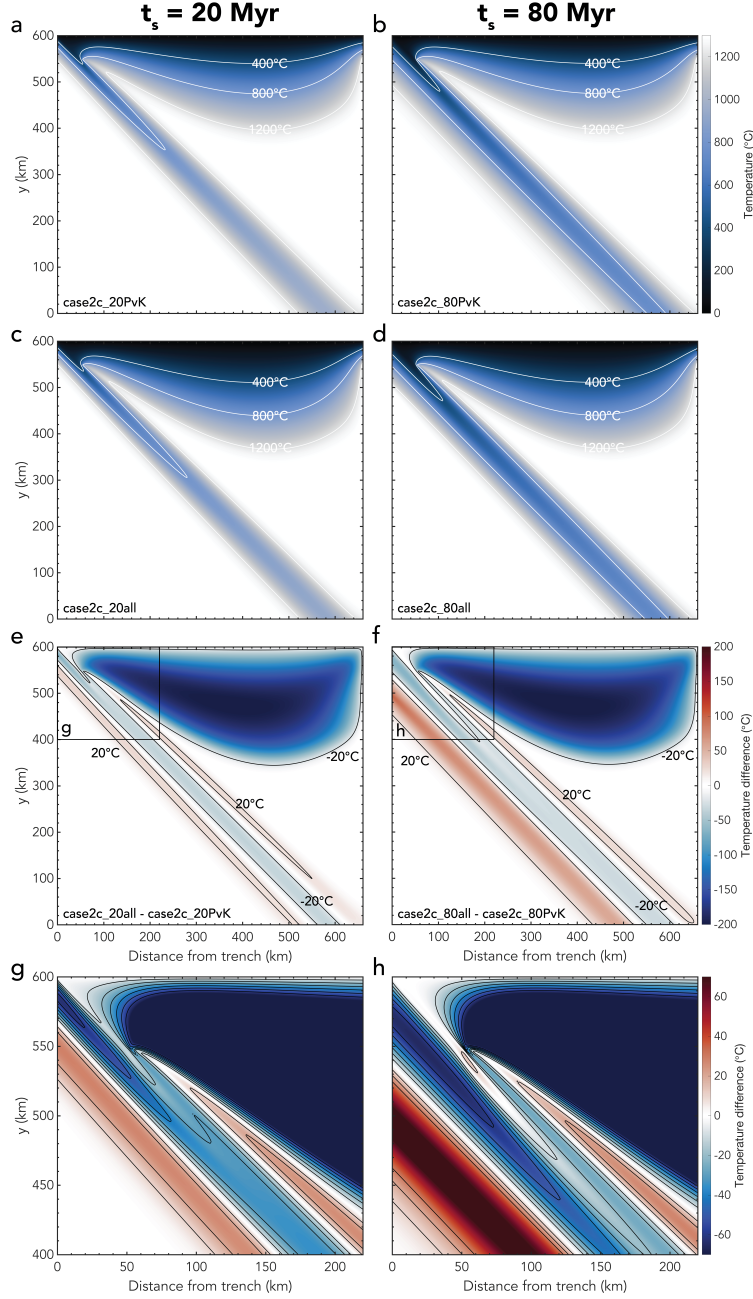


Figure 8. (a-d) Snapshots of the temperature field for models with a slab age of (a,c) 20 Myr and (b,d) 80 Myr with (a,b) constant and (c,d) variable thermal parameters (Table 1). (e-h) Difference in temperature field between (e,g) model case2c.20all and model case2c.20PvK with (g) a zoom of the top left corner of the model. (f,h) Same as panel (e,g) but for a slab age of 80 Myr. Contours of the temperature difference are indicated in black. In panels (g,h) contours for every 10° temperature difference are drawn. Note that panels (g,h) have a different colour scale than panel (e,f) to highlight the differences between the two models within the slab and to easily compare to Figure 6.

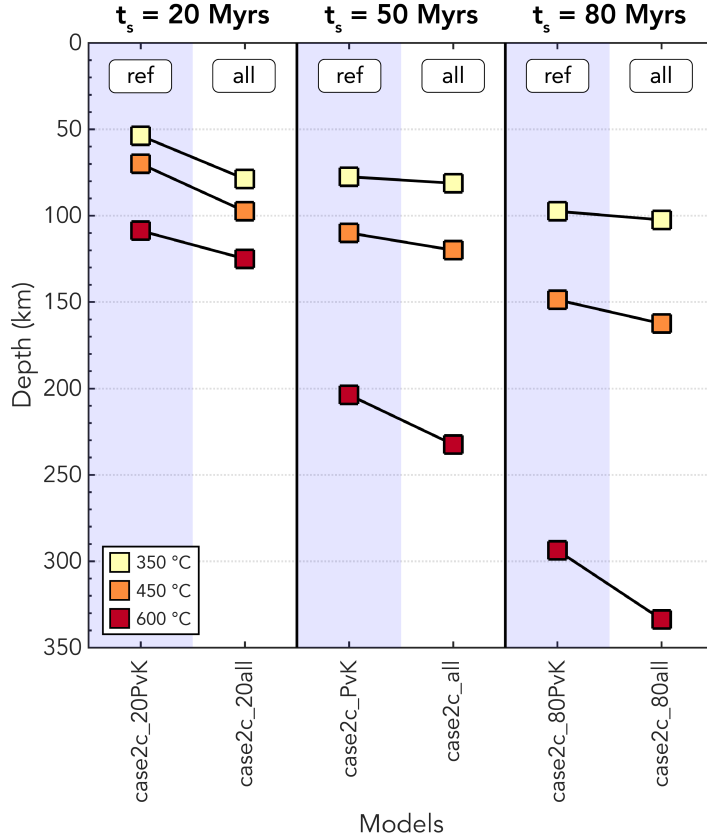


Figure 9. Change in maximum isotherm depth within the slab for end-member models with different subducting plate ages (Table 1). The three isotherm depths plotted here are the same as the ones from the model diagnostics in Table 2. The models with constant values are indicated by ‘ref’.

566 temperature-dependent thermal parameters are used, with implications for the thermo-
 567 chemical changes then ascribed to control intermediate depth seismicity. Depending on
 568 the choices of the functions describing the thermal parameters and their interaction, the
 569 fit with observed seismicity can change. To accurately determine the depth of intermediate-
 570 depth seismicity and the relationship between the thermal structure of the slab and intermediate-
 571 depth seismicity, we recommend the use of temperature-dependent thermal parameters
 572 constrained by the insights on rock behaviour. Neglecting temperature-dependent thermal
 573 parameters could result in significant errors of up to hundreds of kilometres in the
 574 estimated depth of intermediate-depth seismicity or a misinterpretation of the relation
 575 between the thermal structure of a slab and observed intermediate-depth seismicity.

576 *4.1.2 Deep seismicity*

577 The cause of deep earthquakes (>300 km) is hotly debated with proposed mech-
 578 anisms such as dehydration embrittlement, transformational faulting, and (grain size as-
 579 sisted) thermal runaway as a result of shear heating (see Green & Houston, 1995; Frohlich,
 580 2006; Zhan, 2020, for an overview). Regardless of the exact mechanism responsible for
 581 deep earthquakes, it is clear that the thermal structure of the slab plays a large role through
 582 providing the optimal conditions for each of these mechanisms to occur in. In fact, re-
 583 cent studies by Jia et al. (2020); Liu et al. (2021) have shown that local slab tempera-

584 ture likely controls the rupture of deep earthquakes. Our results show that the effect of
 585 using temperature-dependent thermal parameters instead of constant values grows more
 586 pronounced with depth. Therefore, we expect that adding temperature-dependent ther-
 587 mal parameters will significantly affect models of the thermal structure of slabs at depths
 588 between 300–600 km relevant to deep earthquakes.

589 **4.1.3 Megathrust seismicity**

590 Our models here are of limited use in assessing the sensitivity of the temperature
 591 along the shallow interface to the inclusion of temperature-dependent thermal proper-
 592 ties, as (a) in our simplified model geometry, the shallow dip of our interface is signif-
 593 icantly greater than that typically seen in the interface seismogenic zone of most sub-
 594 duction zones (typically $23\pm 8^\circ$ (e.g., Jarrard, 1986; Heuret et al., 2011; Schellart & Rawl-
 595 inson, 2013)); (b) we refrain from including the compositional complexity necessary to
 596 appropriately model the thermal structure of the overriding plate and/or a sedimentary
 597 forearc; and (c) we do not include the effects of shear heating on the shallow interface
 598 P. England (2018).

599 However, noting the impact that the extreme variation in thermal properties at low
 600 temperatures (e.g., Figure 3) has on the rates at which cold material will heat up near
 601 the top of the downgoing plate and in the wedge of the forearc, we recommend using tempera-
 602 ture-dependent thermal parameters in thermal models of subduction zones, in addition to the
 603 other influences mentioned, for when physically realistic estimations of the seismogenic
 604 zone size are desired. Similarly, when observations are linked to the behaviour of the in-
 605 terface (e.g., limits on seismogenesis, on coupling, on slow slip, etc.), the inclusion of tempera-
 606 ture-dependent thermal parameters may alter the inferred mineralogical and rheological con-
 607 trols on such transitions.

608 **4.2 Mineralogical evolution of the slab**

609 As the subducting plate descends, it typically undergoes a range of mineralogical
 610 transitions, relating to the increase in pressure and temperature. These mineralogical
 611 changes, particularly the location at which dehydration reactions may release fluids into
 612 the slab system, play a controlling role in determining the location of intraslab seismic-
 613 ity, and also in influencing a range of other geophysical phenomena, from the internal
 614 impedance and velocity contrasts within the slab (e.g., G. A. Abers, 2000; Rondenay et
 615 al., 2008), to the occurrence of slow slip events on the subduction interface (e.g., Pea-
 616 ccock, 2009), to the development of a hydrated mantle forearc (e.g., G. Abers et al., 2017).
 617 The preservation of volatile-hosting lower-temperature material into the deeper mantle
 618 also plays a role in global geochemical cycles (e.g., Rüpke et al., 2004).

619 Whilst the kinematic constraints we impose on the slab in our models mean there
 620 is little variation in lithostatic pressure between models, we have shown that including
 621 the temperature dependence of thermal parameters in the modelling of slab thermal struc-
 622 tures has an impact on the resultant temperature field. Whilst these changes are small
 623 relative to the total change in temperature experienced by the slab during subduction,
 624 they lead to a slightly different pressure-temperature evolution for the slab material. An
 625 additional crustal layer in our models, which is not included at the moment, would fur-
 626 ther alter the temperature field. However, we note that the changes in the temperature
 627 evolution of the uppermost ~ 8 km of the slab is particularly susceptible to the tem-
 628 perature dependence of thermal properties, given the rapid variation of such values at
 629 cold temperatures (Figure 3). The mineralogical evolution of the shallowest part of the
 630 slab is therefore likely to be altered by the incorporation of temperature-dependent ther-
 631 mal properties, with initially more rapid heating at low pressures giving way to slower
 632 heating at higher pressures, in comparison to models using fixed, temperature-independent
 633 thermal properties. Dehydration reactions in hydrated basaltic oceanic crust typically

634 take place between 350 – 450°C, whilst those in serpentinitised oceanic mantle concen-
 635 trate between 600°C and 800°C (Hacker, Abers, & Peacock, 2003). In linking geophys-
 636 ical observations to thermal models, we again note that the variation in depth of the 350°C
 637 and 450°C isotherms in our models of up to 38.8 km with respect to the reference model
 638 case2c_PvK (Figure 7) would translate for most subduction zones into a significant trench-
 639 perpendicular lateral shift. This will have a significant impact on the source location of
 640 phenomena such as the migration of fluids from the slab to the forearc mantle and/or
 641 updip along the subduction interface.

642 Lastly, the model diagnostics we focus on here centre around the maximum depth
 643 of a given isotherm. However, the variation in thermal structure that we study will also
 644 impact on the thermal cross section of the slab at any given depth - with marginally colder
 645 slabs having a significantly greater volume of material below a given temperature at a
 646 given depth, and hence potentially altering the volatile fluxes within slabs into the mid
 647 mantle.

648 4.3 Model limitations and future work

649 With the exception of a different rheology in the mantle wedge, where we combine
 650 both diffusion and dislocation creep, we use the same model setup as the subduction zone
 651 community benchmark presented by van Keken et al. (2008). We choose this model setup,
 652 as it is well constrained and documented and reproduced by many codes in the geody-
 653 namics community (see codes used in van Keken et al., 2008). Hence, we are able to study
 654 the effect of temperature-dependent thermal parameters on the thermal structure of sub-
 655 duction zones in an isolated, well-constrained manner, although, as discussed, this does
 656 limit their direct applicability to observational data.

657 The model setup is greatly simplified and many complexities that are known to in-
 658 fluence the thermal structure of the slab are ignored. As illustrated in the benchmark
 659 of van Keken et al. (2008) itself, one of the largest influences of thermal structure of the
 660 subducting slab is the employed rheology. The temperature model diagnostics in van Keken
 661 et al. (2008) change up to 189°C when changing from an isoviscous to a dislocation or
 662 diffusion creep rheology. To a lesser extent, the difference between a purely dislocation
 663 creep and diffusion creep rheology is noticeable with variations on the order of 10°C in
 664 model diagnostics. We find that employing a combined dislocation and diffusion creep
 665 rheology does not significantly change the model diagnostics compared to a purely dis-
 666 location or diffusion creep rheology. However, our approximation of combining a dislo-
 667 cation and diffusion creep rheology is simplistic. Using a composite rheology of diffusion
 668 and dislocation creep to properly account for the nonlinearity of the two rheologies would
 669 be more physically appropriate (Ranalli, 1995; Karato, 2008; T. Gerya, 2019). This would
 670 likely introduce changes to the temperature field of the slab on the same order as the
 671 differences observed between a pure diffusion and a pure dislocation model as in van Keken
 672 et al. (2018).

673 Hence, the effect of using temperature-dependent thermal parameters in thermal
 674 models instead of constant values is a secondary effect to rheology when comparing iso-
 675 viscous and non-linear rheologies. However, when comparing non-linear rheologies, us-
 676 ing temperature-dependent thermal parameters instead of constant values will likely have
 677 a greater effect on the thermal structure of the slab than changing the details of the rhe-
 678 ology formulation. Note that these conclusions relate to the thermal structure of the slab;
 679 the rheology plays a major role in the thermal structure of the mantle wedge and over-
 680 riding plate, as evident from the original benchmarks presented in van Keken et al. (2008).

681 Apart from a simplified rheology, we also employ a simplified geometry in our model
 682 setup. Although the model serves as a good benchmark and we can infer some implica-
 683 tions for seismicity from this simple setup, a strictly 45°C dipping slab is not realistic.
 684 In nature the slab dip changes with depth with low dipping angles of $23\pm 8^\circ$ for the megath-

685 rust (Heuret et al., 2011) and larger dip at depth (e.g., Isacks & Barazangi, 1977; King,
686 2001; Cruciani et al., 2005; Syracuse et al., 2010; Klemd et al., 2011; Hu & Gurnis, 2020).
687 Therefore, more realistic models of the thermal structure of subduction zones include
688 these complex geometries (e.g., Syracuse et al., 2010; Van Keken et al., 2012). Our re-
689 sults indicate that in these complex models of the thermal structure of the slab, it is im-
690 portant to take the temperature-dependence of thermal parameters into account as well.
691 Even though including them will likely not change the large-scale subduction evolution,
692 it is important to include the temperature-dependent thermal parameters for accurate
693 comparison with (earthquake) data.

694 Although we focus here on the effect of using temperature-dependent thermal par-
695 ameters, there are numerous other processes relevant to the developing thermal struc-
696 ture of a subduction zone (see van Keken et al., 2019, for an overview). For example, fric-
697 tional (or shear) heating along the plate interface (e.g., Peacock, 1992; Peacock & Wang,
698 1999; Gao & Wang, 2014, 2017) and radiogenic heating in the overriding plate (e.g., Gao
699 & Wang, 2014; P. England, 2018) introduce an additional heat source to the system and
700 result in warmer slabs in line with petrological estimates of the temperatures of rocks
701 in a subduction zone (Penniston-Dorland et al., 2015). Typically these processes are in-
702 cluded in models where a temperature-dependent density formulation is used, although
703 the conductivity and heat capacity are often still taken to be constants. We deliberately
704 do not include these additional heat sources when including the temperature-dependent
705 density to isolate its effect on the thermal structure of a subduction zone. However, we
706 recognise that this may lead to thermodynamic inconsistencies, similar to those intro-
707 duced through inconsistent thermodynamic potentials calculated from the thermal pa-
708 rameters (Schubert et al., 2001; van Zelst et al., 2021). Phase changes, such as serpen-
709 tinisation in the mantle wedge corner (e.g., Hyndman & Peacock, 2003) and the tran-
710 sition from blueschist to hydrous eclogite (e.g., Hacker, Abers, & Peacock, 2003), also
711 play an important role in establishing the thermal structure of the slab, as they are paired
712 with the release of latent heat, density and subsequent volume changes, fluid production
713 and heat advection (see Peacock, 2020, for an overview of petrologic models). Fluid flow
714 and hydrothermal circulation within the upper part of the slab efficiently transport heat
715 updip towards the trench (e.g., Spinelli & Wang, 2008; P. C. England & Katz, 2010; Fac-
716 cenda et al., 2012; Rotman & Spinelli, 2013; R. N. Harris et al., 2017). Depending on
717 the subduction velocity, this can significantly reduce the temperature of the subduction
718 interface (Rotman & Spinelli, 2013). In line with this, processes such as melting and melt
719 transport at the top of the slab and in the mantle wedge corner (e.g., P. C. England &
720 Katz, 2010; Bouilhol et al., 2015; Perrin et al., 2016), magmatism (e.g., Jones et al., 2018),
721 erosion (e.g., Royden, 1993; P. England, 2018), sedimentation (e.g., P. England, 2018),
722 and three-dimensional complexities (e.g., T. V. Gerya, 2011; Wada, 2021) also play a role
723 in the thermal structure of a subduction zone. In addition, subduction is an inherently
724 time-dependent process with the temperature structure of the subducting slab likely chang-
725 ing throughout its evolution which is not captured by the steady-state thermal models
726 presented here (King, 2001; Holt & Condit, 2021). Here, we deliberately choose to ig-
727 nore these complexities to isolate the effect of temperature-dependent thermal param-
728 eters on the thermal structure of the slab. Future studies could focus on these processes
729 to explore their effect on models of the thermal structure of the slab.

730 Lastly, there are numerous functions describing the temperature-dependence of the
731 thermal parameters in the literature and existing functions are continuously updated with
732 improved values for constants to better fit laboratory data. It is outside of the scope of
733 this work to test all different formulations and here we follow McKenzie et al. (2005) and
734 Richards et al. (2018) who used temperature-dependent thermal parameters for plate
735 models of the cooling oceanic lithosphere. However, other possible functions of the tempera-
736 ture-dependence of thermal parameters include formulations from studies like e.g., Berman
737 and Brown (1985); Seipold (1998); A. M. Hofmeister (2007b); Wen et al. (2015); Su et
738 al. (2018).

In addition, the thermal parameters do not merely depend on temperature, but are also dependent on pressure (A. M. Hofmeister, 2007a). We do not consider this pressure-dependence here as we kinematically prescribe the slab and hence do not solve for pressure or velocity within the slab. Studies of the thermal structure of cooling oceanic lithosphere show that the residual misfit with the data reduces upon including the pressure-dependence of the thermal parameters (e.g., Grose & Afonso, 2013; Korenaga & Korenaga, 2016; Richards et al., 2018).

We also restrict our models to a single composition only. We do not include a crustal layer, and we neglect the impact that the mineralogical evolution of the slab will have on the temperature structure, both through the variation in thermal parameters with evolving mineralogy, and through the latent heat of mineralogical transformation.

5 Conclusions

In this work, we look at the effect of adding temperature-dependent thermal parameter in thermal models of subduction zones compared to using constant values.

Using temperature-dependent conductivity decreases the temperature in the slab and results in a larger predicted seismogenic zone width and deeper intermediate-depth seismicity with the maximum depth of the 600°C isotherm changing up to 87.5 km for a model using the thermal conductivity function of (A. Hofmeister, 1999; McKenzie et al., 2005) compared to a reference models with constant values.

Employing a temperature-dependent heat capacity has the opposite effect and results in a warmer slab with a shallower downdip limit of the seismogenic zone and predicted depth of dehydration reactions responsible for intermediate-depth seismicity.

A temperature-dependent density has the least effect on the thermal structure of the slab when compared to the reference model with constant values, although the slab is overall colder. Combining the temperature-dependence of the three thermal parameters negates the effect on the thermal structure of the slab slightly, but the strong cooling of the slab produced by both the temperature-dependent thermal conductivity and density dominates. Therefore, the modelled slab is colder than a slab modelled with constant thermal parameters with, e.g., the maximum depth of the 600°C isotherm changing by 28.8 km. The importance of including temperature-dependent thermal parameters increases for increasing slab age, as the functions of the thermal parameters used in this paper have their most extreme values for lower temperatures.

Even considering the simplifications in our model setup, our results indicate that the changes in the modelled thermal structure of the slab will have important implications on the estimated size of the seismogenic zone in these kinds of thermal models and predictions where intermediate-depth seismicity might occur. For optimal comparison to data and to avoid misinterpretations, we therefore recommend that temperature-dependent thermal parameters are an important modelling ingredient and should be taken into account when using thermal(-mechanical) models of subduction zones.

Acknowledgements

We thank Peter van Keken for providing the original data from van Keken et al. (2008) used to benchmark the code presented here and for providing additional insights on the model setup.

Elements of this work were undertaken on ARC4, part of the High Performance Computing facilities at the University of Leeds, UK. IvZ and TJC were funded by the Royal Society (UK) through University Research Fellowship URF\R1\180088 and Research Fellows Enhancement Award RGF\EA\181084. TJC was also supported through

786 COMET, the UK Natural Environment Research Council's Centre for the Observation
787 and Modelling of Earthquakes, Volcanoes, and Tectonics.

788 Author contribution statement

789 IvZ and TJC conceived the study. IvZ designed and ran the models, analysed the
790 results, and wrote the article. CT and IvZ wrote the code xFieldstone. TJC supervised
791 IvZ and contributed to the analysis of the models. All authors discussed the results and
792 contributed to the model design and the final manuscript.

793 Data availability statement

794 The models were run with the open source xFieldstone (which will be made avail-
795 able on github upon publication). The exact version of the code will be stored in a Zen-
796 do repository. In this repository the data used to reproduce the van Keken et al. (2008)
797 benchmark, the raw data used to produce the figures in this article and the matlab post-
798 processing scripts can be found as well.

799 References

- 800 Abers, G., Van Keken, P., & Hacker, B. (2017). The cold and relatively dry nature
801 of mantle forearcs in subduction zones. *Nature Geoscience*, *10*(5), 333–337.
- 802 Abers, G. A. (2000). Hydrated subducted crust at 100–250 km depth. *Earth and*
803 *Planetary Science Letters*, *176*(3–4), 323–330.
- 804 Abers, G. A., van Keken, P. E., Kneller, E. A., Ferris, A., & Stachnik, J. C. (2006).
805 The thermal structure of subduction zones constrained by seismic imaging:
806 Implications for slab dehydration and wedge flow. *Earth and Planetary Science*
807 *Letters*, *241*(3–4), 387–397.
- 808 Anton Tsitsulin. (2019; retrieved: May 10, 2021). *Optimal qualitative colour palettes*.
809 (<http://tsitsul.in/blog/coloropt/>)
- 810 Arcay, D. (2017). Modelling the interplate domain in thermo-mechanical simulations
811 of subduction: Critical effects of resolution and rheology, and consequences
812 on wet mantle melting. *Physics of the Earth and Planetary Interiors*, *269*,
813 112–132.
- 814 Beall, A., Fagereng, Å., Davies, J. H., Garel, F., & Davies, D. R. (2021). Influence of
815 subduction zone dynamics on interface shear stress and potential relationship
816 with seismogenic behavior. *Geochemistry, Geophysics, Geosystems*, *22*(2),
817 e09267.
- 818 Berman, R. G. (1988). Internally-consistent thermodynamic data for minerals in the
819 system na₂o-k₂o-ca₂o-mg₂o-fe₂o₃-al₂o₃-sio₂-tio₂-h₂o-co₂. *Journal of petrol-*
820 *ogy*, *29*(2), 445–522.
- 821 Berman, R. G., & Aranovich, L. Y. (1996). Optimized standard state and solu-
822 tion properties of minerals: I. Model calibration for olivine, orthopyroxene,
823 cordierite, garnet, and ilmenite in the system FeO-MgO-CaO-Al₂O₃-TiO₂-
824 SiO₂. *Contributions to Mineralogy and Petrology*, *126*(1), 1–24.
- 825 Berman, R. G., & Brown, T. H. (1985). Heat capacity of minerals in the system
826 na₂o k₂o ca₂o mg₂o fe₂o₃ al₂o₃ sio₂ tio₂ h₂o co₂: representation,
827 estimation, and high temperature extrapolation. *Contributions to Mineralogy*
828 *and Petrology*, *89*(2), 168–183.
- 829 Blom, N., Boehm, C., & Fichtner, A. (2017). Synthetic inversions for density us-
830 ing seismic and gravity data. *Geophysical Journal International*, *209*(2), 1204–
831 1220.
- 832 Bouhifd, M. A., Andraut, D., Fiquet, G., & Richet, P. (1996). Thermal expansion of
833 forsterite up to the melting point. *Geophysical research letters*, *23*(10), 1143–
834 1146.

- 835 Bouilhol, P., Magni, V., van Hunen, J., & Kaislaniemi, L. (2015). A numerical ap-
 836 proach to melting in warm subduction zones. , *411*, 37–44.
- 837 Brizzi, S., van Zelst, I., Funicello, F., Corbi, F., & van Dinther, Y. (2020). How
 838 sediment thickness influences subduction dynamics and seismicity. *Journal of*
 839 *Geophysical Research: Solid Earth*, *125*(8), e2019JB018964.
- 840 Chang, C., McNeill, L. C., Moore, J. C., Lin, W., Conin, M., & Yamada, Y. (2010).
 841 In situ stress state in the Nankai accretionary wedge estimated from borehole
 842 wall failures. *Geochemistry, Geophysics, Geosystems*, *11*(12).
- 843 Crameri, F. (2018a). Geodynamic diagnostics, scientific visualisation and StagLab
 844 3.0. *Geoscientific Model Development*, *11*(6), 2541–2562.
- 845 Crameri, F. (2018b). *Scientific colour-maps*. Zenodo. Retrieved from [http://doi](http://doi.org/10.5281/zenodo.1243862)
 846 [.org/10.5281/zenodo.1243862](http://doi.org/10.5281/zenodo.1243862) doi: <http://doi.org/10.5281/zenodo.1243862>
- 847 Crameri, F., Shephard, G. E., & Heron, P. J. (2020). The misuse of colour in science
 848 communication. *Nature communications*, *11*(1), 1–10.
- 849 Crosby, A., McKenzie, D., & Sclater, J. (2006). The relationship between depth,
 850 age and gravity in the oceans. *Geophysical Journal International*, *166*(2), 553–
 851 573.
- 852 Cruciani, C., Carminati, E., & Doglioni, C. (2005). Slab dip vs. lithosphere age: no
 853 direct function. *Earth and Planetary Science Letters*, *238*(3-4), 298–310.
- 854 Denlinger, R. P. (1992). A revised estimate for the temperature structure of the
 855 oceanic lithosphere. *Journal of Geophysical Research: Solid Earth*, *97*(B5),
 856 7219–7222.
- 857 Emmerson, B., & McKenzie, D. (2007). Thermal structure and seismicity of sub-
 858 ducting lithosphere. *Physics of the Earth and Planetary Interiors*, *163*(1-4),
 859 191–208.
- 860 England, P. (2018). On shear stresses, temperatures, and the maximum magni-
 861 tudes of earthquakes at convergent plate boundaries. *Journal of Geophysical*
 862 *Research: Solid Earth*, *123*(8), 7165–7202.
- 863 England, P. C., & Katz, R. F. (2010). Melting above the anhydrous solidus controls
 864 the location of volcanic arcs. *Nature*, *467*(7316), 700–703.
- 865 Faccenda, M., Gerya, T. V., Mancktelow, N. S., & Moresi, L. (2012). Fluid flow
 866 during slab unbending and dehydration: Implications for intermediate-depth
 867 seismicity, slab weakening and deep water recycling. *Geochemistry, Geophysics,*
 868 *Geosystems*, *13*(1).
- 869 Frohlich, C. (2006). Deep earthquakes.
- 870 Fulton, P., Brodsky, E. E., Kano, Y., Mori, J., Chester, F., Ishikawa, T., ... oth-
 871 ers (2013). Low coseismic friction on the Tohoku-Oki fault determined from
 872 temperature measurements. *Science*, *342*(6163), 1214–1217.
- 873 Gao, X., & Wang, K. (2014). Strength of stick-slip and creeping subduction megath-
 874 rusts from heat flow observations. *Science*, *345*(6200), 1038–1041.
- 875 Gao, X., & Wang, K. (2017). Rheological separation of the megathrust seismogenic
 876 zone and episodic tremor and slip. *Nature*, *543*(7645), 416–419.
- 877 Gerya, T. (2019). *Introduction to numerical geodynamic modelling*. Cambridge Uni-
 878 versity Press.
- 879 Gerya, T. V. (2011). Future directions in subduction modeling. *Journal of Geody-*
 880 *namics*, *52*(5), 344–378.
- 881 Gerya, T. V., & Meilick, F. (2011). Geodynamic regimes of subduction under an
 882 active margin: effects of rheological weakening by fluids and melts. *Journal of*
 883 *Metamorphic Geology*, *29*(1), 7–31.
- 884 Green, H. W., & Houston, H. (1995). The mechanics of deep earthquakes. *Annual*
 885 *Review of Earth and Planetary Sciences*, *23*(1), 169–213.
- 886 Grose, C. J., & Afonso, J. C. (2013). Comprehensive plate models for the thermal
 887 evolution of oceanic lithosphere. *Geochemistry, Geophysics, Geosystems*, *14*(9),
 888 3751–3778.
- 889 Gutscher, M.-A., & Peacock, S. M. (2003). Thermal models of flat subduction and

- 890 the rupture zone of great subduction earthquakes. *Journal of Geophysical Re-*
891 *search: Solid Earth*, 108(B1), ESE-2.
- 892 Hacker, B. R., Abers, G. A., & Peacock, S. M. (2003). Subduction factory 1. The-
893 oretical mineralogy, densities, seismic wave speeds, and H₂O contents. *Journal*
894 *of Geophysical Research: Solid Earth*, 108(B1).
- 895 Hacker, B. R., Peacock, S. M., Abers, G. A., & Holloway, S. D. (2003). Subduction
896 factory 2. Are intermediate-depth earthquakes in subducting slabs linked to
897 metamorphic dehydration reactions? *Journal of Geophysical Research: Solid*
898 *Earth*, 108(B1).
- 899 Harris, R., Yamano, M., Kinoshita, M., Spinelli, G., Hamamoto, H., & Ashi, J.
900 (2013). A synthesis of heat flow determinations and thermal modeling along
901 the Nankai Trough, Japan. *Journal of Geophysical Research: Solid Earth*,
902 118(6), 2687–2702.
- 903 Harris, R. N., Spinelli, G. A., & Fisher, A. T. (2017). Hydrothermal circulation
904 and the thermal structure of shallow subduction zones. *Geosphere*, 13(5),
905 1425–1444.
- 906 Herrendörfer, R., Van Dinther, Y., Gerya, T. V., & Dalguer, L. A. (2015). Earth-
907 quake supercycle in subduction zones controlled by the width of the seismo-
908 genic zone. *Nature Geoscience*, 8(6), 471.
- 909 Heuret, A., Lallemand, S., Funiciello, F., Piromallo, C., & Faccenna, C. (2011).
910 Physical characteristics of subduction interface type seismogenic zones revis-
911 ited. *Geochemistry, Geophysics, Geosystems*, 12(1).
- 912 Hillier, J., & Watts, A. (2005). Relationship between depth and age in the north pa-
913 cific ocean. *Journal of Geophysical Research: Solid Earth*, 110(B2).
- 914 Hofmeister, A. (1999). Mantle values of thermal conductivity and the geotherm from
915 phonon lifetimes. *Science*, 283(5408), 1699–1706.
- 916 Hofmeister, A. M. (2007a). Pressure dependence of thermal transport properties.
917 *Proceedings of the National Academy of Sciences*, 104(22), 9192–9197.
- 918 Hofmeister, A. M. (2007b). Thermal conductivity of the earth’s deepest mantle. In
919 *Superplumes: Beyond plate tectonics* (pp. 269–292). Springer.
- 920 Holt, A. F., & Condit, C. B. (2021). Slab temperature evolution over the lifetime of
921 a subduction zone. *Geochemistry, Geophysics, Geosystems*, e2020GC009476.
- 922 Hu, J., & Gurnis, M. (2020). Subduction duration and slab dip. *Geochemistry, Geo-*
923 *physics, Geosystems*, 21(4), e2019GC008862.
- 924 Hyndman, R. D., & Peacock, S. M. (2003). Serpentinization of the forearc mantle.
925 *Earth and Planetary Science Letters*, 212(3-4), 417–432.
- 926 Hyndman, R. D., & Wang, K. (1993). Thermal constraints on the zone of major
927 thrust earthquake failure: The Cascadia subduction zone. *Journal of Geophys-*
928 *ical Research: Solid Earth*, 98(B2), 2039–2060.
- 929 Hyndman, R. D., Yamano, M., & Oleskevich, D. A. (1997). The seismogenic zone of
930 subduction thrust faults. *Island Arc*, 6(3), 244–260.
- 931 Isacks, B. L., & Barazangi, M. (1977). Geometry of Benioff zones: Lateral segmen-
932 tation and downwards bending of the subducted lithosphere. *Island Arcs, Deep*
933 *Sea Trenches and Back-Arc Basins*, 1, 99–114.
- 934 Jarrard, R. D. (1986). Relations among subduction parameters. *Reviews of Geo-*
935 *physics*, 24(2), 217–284.
- 936 Jia, Z., Shen, Z., Zhan, Z., Li, C., Peng, Z., & Gurnis, M. (2020). The 2018 Fiji Mw
937 8.2 and 7.9 deep earthquakes: One doublet in two slabs. *Earth and Planetary*
938 *Science Letters*, 531, 115997.
- 939 Jones, D. W. R., Katz, R. F., Tian, M., & Rudge, J. F. (2018). Thermal impact
940 of magmatism in subduction zones. *Earth and Planetary Science Letters*, 481,
941 73–79.
- 942 Jung, H., Green II, H. W., & Dobrzhinetskaya, L. F. (2004). Intermediate-depth
943 earthquake faulting by dehydration embrittlement with negative volume
944 change. *Nature*, 428(6982), 545–549.

- 945 Karato, S.-i. (2008). Deformation of earth materials. *An Introduction to the Rheol-*
 946 *ogy of Solid Earth*, 463.
- 947 Kelemen, P. B., & Hirth, G. (2007). A periodic shear-heating mechanism for
 948 intermediate-depth earthquakes in the mantle. *Nature*, 446(7137), 787–790.
- 949 King, S. D. (2001). Subduction zones: observations and geodynamic models. *Physics*
 950 *of the Earth and Planetary Interiors*, 127(1-4), 9–24.
- 951 Klemm, R., John, T., Scherer, E., Rondenay, S., & Gao, J. (2011). Changes in dip
 952 of subducted slabs at depth: petrological and geochronological evidence from
 953 hp–uhp rocks (Tianshan, NW-China). *Earth and Planetary Science Letters*,
 954 310(1-2), 9–20.
- 955 Korenaga, T., & Korenaga, J. (2016). Evolution of young oceanic lithosphere and
 956 the meaning of seafloor subsidence rate. *Journal of Geophysical Research:*
 957 *Solid Earth*, 121(9), 6315–6332.
- 958 Liu, H., Gurnis, M., Leng, W., Jia, Z., & Zhan, Z. (2021). Tonga slab morphology
 959 and stress variations controlled by a relic slab: Implications for deep earth-
 960 quakes in the Tonga-Fiji region. *Geophysical Research Letters*, e2020GL091331.
- 961 McKenzie, D., Jackson, J., & Priestley, K. (2005). Thermal structure of oceanic and
 962 continental lithosphere. *Earth and Planetary Science Letters*, 233(3-4), 337–
 963 349.
- 964 McKenzie, D., & Sclater, J. (1969). Heat flow in the eastern Pacific and sea floor
 965 spreading. *Bulletin Volcanologique*, 33(1), 101–117.
- 966 Parsons, B., & Sclater, J. G. (1977). An analysis of the variation of ocean floor
 967 bathymetry and heat flow with age. *Journal of Geophysical Research*, 82(5),
 968 803–827.
- 969 Peacock, S. M. (1992). Blueschist-facies metamorphism, shear heating, and p-t-t
 970 paths in subduction shear zones. *Journal of Geophysical Research: Solid Earth*,
 971 97(B12), 17693–17707.
- 972 Peacock, S. M. (1993). Large-scale hydration of the lithosphere above subducting
 973 slabs. *Chemical Geology*, 108(1-4), 49–59.
- 974 Peacock, S. M. (2001). Are the lower planes of double seismic zones caused by ser-
 975 pentine dehydration in subducting oceanic mantle? *Geology*, 29(4), 299–302.
- 976 Peacock, S. M. (2009). Thermal and metamorphic environment of subduction
 977 zone episodic tremor and slip. *Journal of Geophysical Research: Solid Earth*,
 978 114(B8).
- 979 Peacock, S. M. (2020). Advances in the thermal and petrologic modeling of subduc-
 980 tion zones. *Geosphere*, 16(4), 936–952.
- 981 Peacock, S. M., & Hyndman, R. D. (1999). Hydrous minerals in the mantle wedge
 982 and the maximum depth of subduction thrust earthquakes. *Geophysical Re-*
 983 *search Letters*, 26(16), 2517–2520.
- 984 Peacock, S. M., & Wang, K. (1999). Seismic consequences of warm versus cool sub-
 985 duction metamorphism: Examples from southwest and northeast Japan. *Sci-*
 986 *ence*, 286(5441), 937–939.
- 987 Penniston-Dorland, S. C., Kohn, M. J., & Manning, C. E. (2015). The global range
 988 of subduction zone thermal structures from exhumed blueschists and eclogites:
 989 Rocks are hotter than models. *Earth and Planetary Science Letters*, 428,
 990 243–254.
- 991 Perrin, A., Goes, S., Prytulak, J., Davies, D. R., Wilson, C., & Kramer, S. (2016).
 992 Reconciling mantle wedge thermal structure with arc lava thermobaromet-
 993 ric determinations in oceanic subduction zones. *Geochemistry, Geophysics,*
 994 *Geosystems*, 17(10), 4105–4127.
- 995 Petrini, C., Gerya, T., Yarushina, V., van Dinther, Y., Connolly, J., & Madonna, C.
 996 (2020). Seismo-hydro-mechanical modelling of the seismic cycle: methodology
 997 and implications for subduction zone seismicity. *Tectonophysics*, 791, 228504.
- 998 Ponko, S. C., & Peacock, S. M. (1995). Thermal modeling of the southern Alaska
 999 subduction zone: insight into the petrology of the subducting slab and overly-

- ing mantle wedge. *Journal of Geophysical Research: Solid Earth*, 100(B11), 22117–22128.
- Pozgay, S. H., Wiens, D. A., Conder, J. A., Shiobara, H., & Sugioka, H. (2009). Seismic attenuation tomography of the mariana subduction system: Implications for thermal structure, volatile distribution, and slow spreading dynamics. *Geochemistry, Geophysics, Geosystems*, 10(4).
- Press, W. H., Teukolsky, S. A., Vetterling, W. T., & Flannery, B. P. (1992). Numerical recipes in c++. *The art of scientific computing*, 2, 1002.
- Ranalli, G. (1995). *Rheology of the earth*. Springer Science & Business Media.
- Richards, F., Hoggard, M., Cowton, L., & White, N. (2018). Reassessing the thermal structure of oceanic lithosphere with revised global inventories of basement depths and heat flow measurements. *Journal of Geophysical Research: Solid Earth*, 123(10), 9136–9161.
- Rondenay, S., Abers, G. A., & Van Keken, P. E. (2008). Seismic imaging of subduction zone metamorphism. *Geology*, 36(4), 275–278.
- Rotman, H. M., & Spinelli, G. A. (2013). Global analysis of the effect of fluid flow on subduction zone temperatures. *Geochemistry, Geophysics, Geosystems*, 14(8), 3268–3281.
- Royden, L. H. (1993). The steady state thermal structure of eroding orogenic belts and accretionary prisms. *Journal of Geophysical Research: Solid Earth*, 98(B3), 4487–4507.
- Rüpke, L. H., Morgan, J. P., Hort, M., & Connolly, J. A. (2004). Serpentine and the subduction zone water cycle. *Earth and Planetary Science Letters*, 223(1–2), 17–34.
- Schellart, W. P., & Rawlinson, N. (2013). Global correlations between maximum magnitudes of subduction zone interface thrust earthquakes and physical parameters of subduction zones. *Physics of the Earth and Planetary Interiors*, 225, 41–67.
- Schmeling, H., Babeyko, A., Enns, A., Faccenna, C., Funiciello, F., Gerya, T., . . . others (2008). A benchmark comparison of spontaneous subduction models—towards a free surface. *Physics of the Earth and Planetary Interiors*, 171(1–4), 198–223.
- Scholz, C. H. (2019). *The mechanics of earthquakes and faulting*. Cambridge university press.
- Schubert, G., Turcotte, D. L., & Olson, P. (2001). *Mantle convection in the earth and planets 2 volume set*. Cambridge University Press.
- Sclater, J., Jaupart, C., & Galson, D. (1980). The heat flow through oceanic and continental crust and the heat loss of the earth. *Reviews of Geophysics*, 18(1), 269–311.
- Seipold, U. (1998). Temperature dependence of thermal transport properties of crystalline rocks—a general law. *Tectonophysics*, 291(1–4), 161–171.
- Spinelli, G. A., & Wang, K. (2008). Effects of fluid circulation in subducting crust on nankai margin seismogenic zone temperatures. *Geology*, 36(11), 887–890.
- Stein, C. A., & Stein, S. (1994). Constraints on hydrothermal heat flux through the oceanic lithosphere from global heat flow. *Journal of Geophysical Research: Solid Earth*, 99(B2), 3081–3095.
- Su, C., Liu, Y., Song, W., Fan, D., Wang, Z., & Tang, H. (2018). Thermodynamic properties of san carlos olivine at high temperature and high pressure. *Acta Geochimica*, 37(2), 171–179.
- Syracuse, E. M., van Keken, P. E., & Abers, G. A. (2010). The global range of subduction zone thermal models. *Physics of the Earth and Planetary Interiors*, 183(1–2), 73–90.
- Turcotte, D., & Schubert, G. (2002). *Geodynamics*. Cambridge University Press.
- van Dinther, Y., Gerya, T. V., Dalguer, L. A., Corbi, F., Funiciello, F., & Mai, P. M. (2013). The seismic cycle at subduction thrusts: 2. Dynamic implica-

- 1055 tions of geodynamic simulations validated with laboratory models. *Journal of*
 1056 *Geophysical Research: Solid Earth*, *118*(4), 1502–1525.
- 1057 van Dinther, Y., Gerya, T. V., Dalguer, L. A., Mai, P. M., Morra, G., & Giardini,
 1058 D. (2013). The seismic cycle at subduction thrusts: Insights from seismo-
 1059 thermo-mechanical models. *Journal of Geophysical Research: Solid Earth*,
 1060 *118*(12), 6183–6202.
- 1061 van Dinther, Y., Mai, P. M., Dalguer, L. A., & Gerya, T. V. (2014). Modeling the
 1062 seismic cycle in subduction zones: The role and spatiotemporal occurrence of
 1063 off-megathrust earthquakes. *Geophysical Research Letters*, *41*(4), 1194–1201.
- 1064 Van Keken, P., Kita, S., & Nakajima, J. (2012). Thermal structure and
 1065 intermediate-depth seismicity in the tohoku-hokkaido subduction zones. *Solid*
 1066 *Earth*, *3*(2), 355–364.
- 1067 van Keken, P. E., Currie, C., King, S. D., Behn, M. D., Cagnioncle, A., He, J., ...
 1068 others (2008). A community benchmark for subduction zone modeling. *Physics*
 1069 *of the Earth and Planetary Interiors*, *171*(1-4), 187–197.
- 1070 van Keken, P. E., Hacker, B. R., Syracuse, E. M., & Abers, G. A. (2011). Subduc-
 1071 tion factory: 4. Depth-dependent flux of H₂O from subducting slabs world-
 1072 wide. *Journal of Geophysical Research: Solid Earth*, *116*(B1).
- 1073 van Keken, P. E., Kiefer, B., & Peacock, S. M. (2002). High-resolution models
 1074 of subduction zones: Implications for mineral dehydration reactions and the
 1075 transport of water into the deep mantle. *Geochemistry, Geophysics, Geosys-*
 1076 *tems*, *3*(10), 1–of.
- 1077 van Keken, P. E., Wada, I., Abers, G. A., Hacker, B. R., & Wang, K. (2018). Mafic
 1078 high-pressure rocks are preferentially exhumed from warm subduction settings.
 1079 *Geochemistry, Geophysics, Geosystems*, *19*(9), 2934–2961.
- 1080 van Keken, P. E., Wada, I., Sime, N., & Abers, G. A. (2019). Thermal structure
 1081 of the forearc in subduction zones: A comparison of methodologies. *Geochem-*
 1082 *istry, Geophysics, Geosystems*, *20*(7), 3268–3288.
- 1083 van Zelst, I., Cramer, F., Pusok, A. E., Glerum, A., Dannberg, J., & Thieulot,
 1084 C. (2021). 101 Geodynamic modelling: How to design, carry out, and
 1085 interpret numerical studies. *Solid Earth Discussions*, *2021*, 1–80. Re-
 1086 trieved from <https://se.copernicus.org/preprints/se-2021-14/> doi:
 1087 10.5194/se-2021-14
- 1088 Van Zelst, I., Wollherr, S., Gabriel, A.-A., Madden, E. H., & van Dinther, Y. (2019).
 1089 Modeling megathrust earthquakes across scales: One-way coupling from geo-
 1090 dynamics and seismic cycles to dynamic rupture. *Journal of Geophysical*
 1091 *Research: Solid Earth*, *124*(11), 11414–11446.
- 1092 Wada, I. (2021). A simple picture of mantle wedge flow patterns and temperature
 1093 variation. *Journal of Geodynamics*, 101848.
- 1094 Wang, J., Zhao, D., & Yao, Z. (2017). Seismic anisotropy evidence for dehydration
 1095 embrittlement triggering intermediate-depth earthquakes. *Scientific reports*,
 1096 *7*(1), 1–9.
- 1097 Wen, H., Lu, J.-h., Xiao, Y., & Deng, J. (2015). Temperature dependence of ther-
 1098 mal conductivity, diffusion and specific heat capacity for coal and rocks from
 1099 coalfield. *Thermochimica acta*, *619*, 41–47.
- 1100 Xu, Y., Shankland, T. J., Linhardt, S., Rubie, D. C., Langenhorst, F., & Klasinski,
 1101 K. (2004). Thermal diffusivity and conductivity of olivine, wadsleyite and ring-
 1102 woodite to 20 gpa and 1373 k. *Physics of the Earth and Planetary Interiors*,
 1103 *143*, 321–336.
- 1104 Yabe, S., Fukuchi, R., Hamada, Y., & Kimura, G. (2019). Simultaneous estimation
 1105 of in situ porosity and thermal structure from core sample measurements and
 1106 resistivity log data at nankai accretionary prism. *Earth, Planets and Space*,
 1107 *71*(1), 1–15.
- 1108 Yamasaki, T., & Seno, T. (2003). Double seismic zone and dehydration embrit-
 1109 tlement of the subducting slab. *Journal of Geophysical Research: Solid Earth*,

1110 108(B4).
1111 Zhan, Z. (2020). Mechanisms and implications of deep earthquakes. *Annual Review*
1112 *of Earth and Planetary Sciences*, 48, 147–174.